



Chaos Synchronization and Chaos Control Based on Kannan Mappings

S. Sh. Alaviani

Department of Electrical Engineering, Amirkabir University of Technology,
Tehran, Iran

E-mail: shaho@aut.ac.ir

Abstract: In this paper, a new method for constructing chaotically synchronizing systems is proposed. Furthermore, a new control method for stabilizing a periodic orbit embedded in a chaotic attractor is proposed. The validity of these methods is shown by a property of Kannan mappings. It is shown that in some cases in which method of contraction mappings, proposed by Ushio (T. Ushio. Chaotic Synchronization and Controlling Chaos Based on Contraction Mappings, *Physics Letters A*, vol. 198, 14-22, 1995.), cannot be applied to synchronize or control of chaotic systems, the method may be applied. Ultimately, a numerical example is given in order to present the results established.

Keywords: chaos synchronization, chaos control, Kannan mappings.

1. Introduction

Chaos, as a very interesting nonlinear phenomenon, has been intensively studied over the past decades. Dynamic chaos has aroused considerable interest in many areas of science and technology due to its powerful applications in chemical reactions, power converters, biological systems, information processing, secure communication, neural networks etc. In the study of chaotic systems, chaos synchronization and chaos control play a very important role and have great significance in the application of chaos.

Chaos synchronization seems to be difficult to observe in physical systems because chaotic behavior is very sensitive to both the initial conditions and noise. However, Pecora and Carroll [1] have successfully proposed a method to synchronize two identical chaotic systems with different initial conditions. Since then, a variety of approaches have been proposed for the synchronization of chaotic systems which include contraction mappings [2], variable structure control [3,4], parameters adaptive control [5,6], observer based control [7,8], nonlinear control [9-11], nonlinear replacement control [12], variable strength linear coupling control [13], active control [14,15] and so on.

On the other hand, chaos control is a very attractive subject in the study of chaotic systems. Since the method for controlling of chaos was first proposed by Ott et al [16], many chaos control methods have been developed extensively over the past decades such as contraction mappings [2], chaotic targeting method [17,18], delayed feedback control [19] etc. Yu et al [20] used the contraction mapping method, proposed by Ushio [2], to stabilize chaotic discrete neural networks.



Neural networks have been widely used as models of real neural structures from small networks of neurons to large scale neurosystem. In recent years, investigation of chaotic dynamics in neural networks becomes an active field in the study of neural networks dynamics. Numerous chaotic neural network models have been proposed for investigation [20-22]. Among the spectrum of applications of chaos control, neural system is a particularly interesting research object of complex structures that it can be applied [23,24].

In this paper, a new method for synthesis of chaotically synchronizing systems based on Kannan mappings is proposed. Also, a new method based on these mappings to stabilize chaotic discrete systems is proposed. These methods are applied to synchronize and control chaotic discrete neural networks. A similar advantage of the methods proposed in this paper and the methods proposed by Ushio [2] is that the linearization of the system near the stabilized orbit is not required. However, in some cases in which the proposed methods of Ushio [2] are not applicable to synchronize or control chaotic systems, the methods may be applied.

This paper is organized as follows. In section 2, problem of chaos synchronization is studied. In section 3, problem of controlling chaos is discussed. Eventually, a numerical example is given in order to present the result investigated.

2. Chaos Synchronization

First, the following theorem which Kannan proved in 1969 is introduced.

Theorem [25] Let (X, d) be a complete metric space. Let T be a Kannan mapping on X , that is, there exists $\alpha \in [0, \frac{1}{2})$ such that

$$d(Tx, Ty) \leq \alpha(d(Tx, x) + d(Ty, y))$$

for all $x, y \in X$. Then, there exists a unique fixed point $x_0 \in X$ of T .

We now consider chaotic discrete-time systems described by

$$x(k+1) = f(x(k)), \quad (1)$$

where $x(k) \in \mathbb{R}^n$ is the state of the system at time k , and f is a mapping from \mathbb{R}^n to itself. We assume that f is rewritten as follows

$$f := g + h, \quad (2)$$

where both g and h are mappings from \mathbb{R}^n to itself and g is a Kannan mapping on a closed set $\Omega \in \mathbb{R}^n$. It is assumed that a chaotic attractor \mathcal{A} of Eq. (1) is in Ω . Many methods for constructing synchronized chaotic systems are based upon the decomposition of states of chaotic systems, and it is proved by using conditional Lyapunov exponents whether the constructed systems are synchronized. Ushio proposes a method based on the partition of the nonlinear mapping, and synchronization of the constructed systems is guaranteed by a property of contraction mappings.

This paper proposes another method based on partitioning of the nonlinear mapping, and synchronization of the constructed systems is guaranteed by a



property of Kannan mappings. In the following subsections, we study synthesis methods for in-phase and anti-phase synchronization of chaotic systems.

2.1 In-phase synchronization

That the difference of the states of two systems converges to zero is called in-phase synchronization or synchronization. We construct a system described by

$$w(k+1) = g(w(k)) + h(x(k)) , \quad (3)$$

where $w(k) \in \mathbb{R}^n$ is the state of the system, and $x(k) \in \mathbb{R}^n$ is the state of Eq. (1). Suppose that initial state $x(0)$ of Eq. (1) is in the basin of the attractor \mathcal{A} , and both states $x(k)$ and $w(k)$ of Eq. (1) and (3) are in Ω for each $k \in \mathbb{N}$, where \mathbb{N} denotes the set of all natural numbers. We assume that there exist a closed set $\Omega \in \mathbb{R}^n$ and a nonnegative constant $0 \leq \alpha < \frac{1}{2}$ such that for any $x, y \in \Omega$ the mapping g satisfies

$$\|g(x) - g(y)\| \leq \alpha(\|x - g(x)\| + \|y - g(y)\|) .$$

We show that Eq. (1) and (3) are in-phase synchronized, so

$$\begin{aligned} \|x(k+1) - w(k+1)\| &= \|g(x(k)) - g(w(k))\| \\ &\leq \alpha(\|x(k) - g(x(k))\| + \|w(k) - g(w(k))\|) . \end{aligned}$$

According to Theorem, we obtain

$$\lim_{k \rightarrow \infty} \|x(k) - w(k)\| = 0 .$$

Thus, in-phase chaotic synchronization of Eqs. (1) and (3) is achieved. Note that $w(0)$ is not necessarily in the basin of \mathcal{A} .

Let us consider the following fully connected network composed of m -neurons, as given in [20]:

$$x_{k+1}^i = \varphi_\mu \left(\sum_{j=1}^m W_{ij} x_k^j \right) , \quad i = 1, 2, \dots, m$$

where $\varphi_\mu(z) = (1 + e^{-\mu z})^{-1}$ is assumed to be the sigmoid function. Let $m = 2$, i.e., consider the case where we have a 2D fully connected neural network defined as

$$\begin{aligned} x_{k+1} &= \varphi_\mu(w_{11}x_k + w_{12}y_k) \cdot (4 - a) \\ y_{k+1} &= \varphi_\mu(w_{21}x_k + w_{22}y_k) \cdot (4 - a) \end{aligned}$$

Altering the matrix $W = (w_{ij})$ of connecting, this map can generate various complex dynamical patterns, including deterministic chaos [23]. We start our study with a 2D neural network with matrix

$$W = \begin{pmatrix} -a & a \\ -b & b \end{pmatrix} .$$

This simplified neural network is dynamically equivalent to a one-parameter family of s-unimodal maps; it is well known that this map will generate chaotic via the Feigenbaum scenario.

We partition the neural network as follows

$$h(x_k, y_k) = \begin{pmatrix} \varphi_\mu(w_{11}x_k + w_{12}y_k) - \sqrt{|x_k|} & 0 \\ 0 & \varphi_\mu(w_{21}x_k + w_{22}y_k) - \sqrt{|y_k|} \end{pmatrix} ,$$



$$g(x_k, y_k) = \begin{pmatrix} \sqrt{|x_k|} & 0 \\ 0 & \sqrt{|y_k|} \end{pmatrix}.$$

The mapping g satisfies Kannan mapping for any $x, y \in \mathbb{R}$. Then, we have the following new system

$$\begin{aligned} w_1(k+1) &= \varphi_\mu(w_{11}x_k + w_{12}y_k) - \sqrt{|x_k|} + \sqrt{|w_1(k)|}, (5-a) \\ w_2(k+1) &= \varphi_\mu(w_{21}x_k + w_{22}y_k) - \sqrt{|y_k|} + \sqrt{|w_2(k)|}, (5-b) \end{aligned}$$

So in-phase synchronization of System (4) and System (5) is achieved.

Remark 1 Because $\sqrt{|x|}$, $x \in \mathbb{R}$, is not contraction mapping, the results given in [2] are not applicable to show the synchronization of System (4) and System (5).

2.2 Anti-phase synchronization

That the states of synchronized systems have the same absolute values but opposite signs is called anti-phase synchronization. We can say that anti-phase synchronization holds if

$$\lim_{k \rightarrow \infty} \|x_1(k) + x_2(k)\| = 0,$$

where $x_i, i = 1, 2$, is the state of the system. Suppose that the state $x(k)$ is both in the basin of the chaotic attractor \mathcal{A} and in Ω , and $w(k)$ is in Ω . Then,

$$\begin{aligned} \|x(k+1) + w(k+1)\| &= \|g(x(k)) + g(w(k))\| \\ &\leq \alpha(\|x(k) + g(x(k))\| + \|w(k) + g(w(k))\|) \end{aligned}$$

According to Theorem, we obtain

$$\lim_{k \rightarrow \infty} \|x(k) + w(k)\| = 0.$$

Thus, anti-phase chaotic synchronization of $x(k)$ and $w(k)$ is achieved.

3. Chaos Control

Consider the following chaotic discrete-time systems with an external input

$$Z_{k+1} = f(Z_k) + Bu_k, \quad (6)$$

where $Z_k \in \mathbb{R}^n$ and $u_k \in \mathbb{R}^l$ are the state and input of the system, and B is an $n \times l$ constant matrix. Eq. (6) without input has a chaotic attractor A . Let $Z^* = f(Z^*)$ be a periodic orbit embedded in A . We consider the following input

$$u_k = \begin{cases} D(z_k) - D(z^*) & \text{if } \|z_k - z^*\| < \epsilon \\ 0 & \text{otherwise} \end{cases}, \quad (7)$$

where D is a mapping from \mathbb{R}^n to \mathbb{R}^l , and ϵ is a sufficiently small positive constant. Assume that the mapping $f + BD$ is a Kannan mapping on a closed set $\Omega \in \mathbb{R}^n$, and the chaotic attractor A is within Ω . Suppose that the initial state z_0 of Eq.(6) is within Ω ; then, the following behavior z_k controlled by Eq.(7) is expected

$$\begin{aligned} \|z_{k+1} - z^*\| &= \|(f + BD)z_k - (f + BD)z^*\| \\ &\leq \alpha(\|z_k - (f + BD)z_k\| + \|z^* - (f + BD)z^*\|). \end{aligned}$$

Since $0 \leq \alpha < \frac{1}{2}$, according to Theorem, we get $\lim_{t \rightarrow \infty} \|z_k - z^*\| = 0$, and the periodic orbit z^* can be stabilized in Ω .



As in [20], we consider the neural network defined as follows:

$$x_{k+1} = \varphi_{\mu}(w_{11}x_k + w_{12}y_k) + u_{1k}, \quad (8-a)$$

$$y_{k+1} = \varphi_{\mu}(w_{21}x_k + w_{22}y_k) + u_{2k}, \quad (8-b)$$

where $u_{1k}, u_{2k} \in \mathbb{R}$ are control inputs. Then, we have

$$z_k = \begin{pmatrix} x_k \\ y_k \end{pmatrix}, f(x_k, y_k) = \begin{pmatrix} \varphi_{\mu}(w_{11}x_k + w_{12}y_k) \\ \varphi_{\mu}(w_{21}x_k + w_{22}y_k) \end{pmatrix}, \text{ and } B = \begin{pmatrix} 1 & 0 \\ 0 & 1 \end{pmatrix}.$$

Now, let us consider the following mapping

$$D(x_k, y_k) = \begin{pmatrix} -\varphi_{\mu}(w_{11}x_k + w_{12}y_k) + \sqrt{|x_k|} \\ -\varphi_{\mu}(w_{21}x_k + w_{22}y_k) + \sqrt{|y_k|} \end{pmatrix}.$$

Then, the mapping $f + BD$ is a Kannan mapping. Thus, the following control input can stabilize any periodic orbit embedded in a chaotic attractor of (6)

$$u_k = \begin{cases} \begin{pmatrix} u_{1k} \\ u_{2k} \end{pmatrix} = \begin{pmatrix} -\varphi_{1\mu}(x_k, y_k) + \sqrt{|x_k|} + \varphi_{1\mu}(x^*, y^*) - \sqrt{|x^*|} \\ -\varphi_{2\mu}(x_k, y_k) + \sqrt{|y_k|} + \varphi_{2\mu}(x^*, y^*) - \sqrt{|y^*|} \end{pmatrix} & \text{if } \|z_k - z^*\| < \epsilon \\ 0 & \text{otherwise} \end{cases}$$

where $z^* = (x^*, y^*)$ denotes a stabilized periodic state with period 1. To obtain the necessary information of an approximate location of the desired periodic orbit, the strategy described in Ref. [26] is utilized. We collect a long data string of observed $z_1, z_2 = f(z_1)$ and so on. If two successive z_s are closed to each other, say z_{100} and z_{101} , then there will typically be a period-1 orbit z^* nearby. Having observed a first such close return pair, we then search the succeeding data for other close return pairs (z_k, z_{k+1}) restricted to the small region of the original close return. Because orbits on a strange attractor are ergodic, we will get many such pairs if the data string is long enough. When the first close return pair is detected, the first point of the pair is taken as a reference point. There are a number of close return pairs detected, which are close to reference point, where $z_{j,1}$ and $z_{j,2}$ are respectively used to denote the first point and its successive point of the j th collected return pair, $j = 1, 2, \dots, M$, where M is the maximum number of collected return pairs. The mean value

$$z^* = \frac{1}{2M} \sum_{j=1}^M (z_{j,1} + z_{j,2}), \quad (9)$$

is regarded as an approximate fixed point z^* . This fixed point can be used to define a neighborhood $|z_i - z^*| \leq \epsilon$ in which control input is activated.

Remark 2 In comparison with the results given in [20], it can be seen that using controller u_k , proposed in this section, the results of [20] cannot show the control of the chaotic discrete neural network.



4. Numerical Example

Consider the following chaotic neural network

$$x_{k+1} = \varphi_{\mu}(-5x_k + 5y_k) + u_{1k} , \quad (10 - a)$$

$$y_{k+1} = \varphi_{\mu}(-25x_k + 25y_k) + u_{2k} , \quad (10 - b)$$

where $\varphi_{\mu}(z) = (1 + e^{-\mu z})^{-1}$ is assumed to be the sigmoid function. The system has chaotic behavior for $\mu = 5.5$, and the approximate period-3 orbit is estimated at $(0.999496, 1.00000)^T$, $(0.593963, 0.870103)^T$, and $(0.503459, 0.517291)^T$, when the condition $|z_i - z_{i+3}| \leq 0.005$ is satisfied [20].

We first show the simulation results of chaotically synchronizing System (10) and System (5) without control input. So System (5) becomes as follows

$$w_1(k+1) = \varphi_{\mu}(-5x(k) + 5y(k)) - \sqrt{|x(k)|} + \sqrt{|w_1(k)|} , \quad (11 - a)$$

$$w_2(k+1) = \varphi_{\mu}(-25x(k) + 25y(k)) - \sqrt{|y(k)|} + \sqrt{|w_2(k)|} . \quad (11 - b)$$

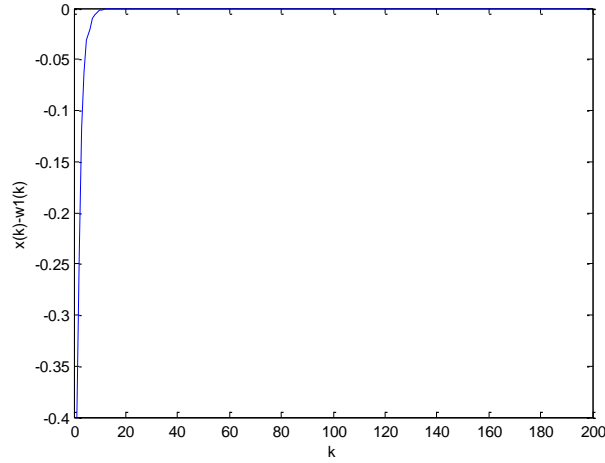


Fig. 1 The error $x(k) - w_1(k)$

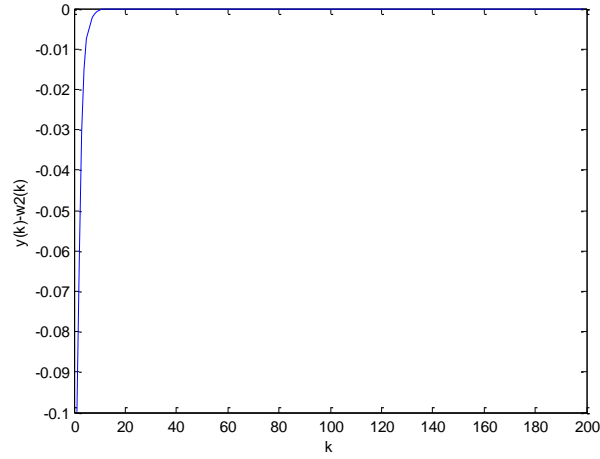


Fig. 2 The error $y(k) - w_2(k)$

The system is simulated with initial conditions $x(0) = 0.5, y(0) = 0.6, w_1(0) = 0.9, w_2(0) = 0.7$, and the differences are showed in Figs. (1) and (2). These figures show that system (10) is synchronized with system (11).

Now, we show the simulation results of chaos control of System (10) using controller u_k proposed in previous section.

Behaviors of the state variables x and y and the input controls u_1 and u_2 are shown in Figs. 3-6, when a periodic orbit with period=3 is stabilized with $\epsilon = 0.002$.

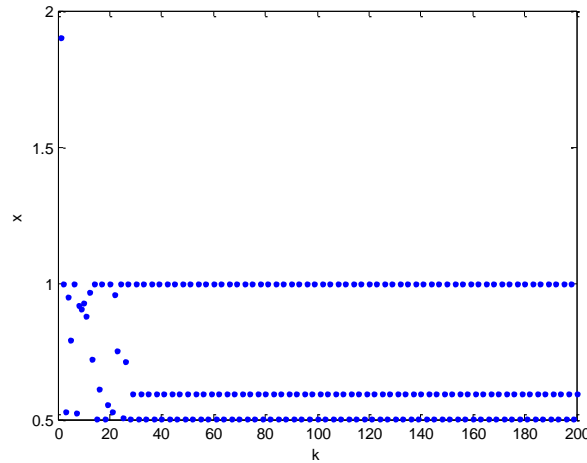




Fig. 3

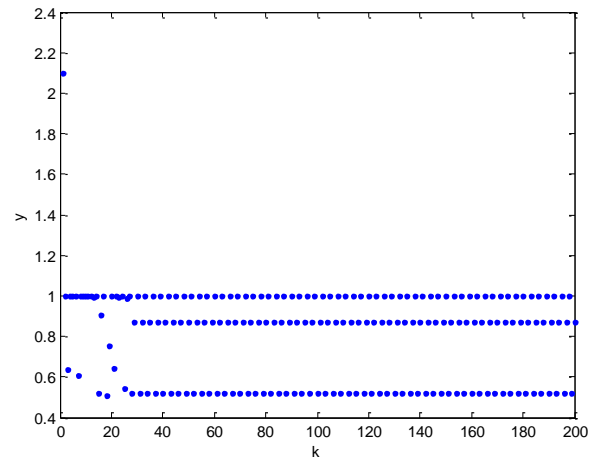


Fig. 4

Figs.3 and 4 show behaviors of the state variables x and y , respectively, with initial condition $(1.9 \ 2.1)^T$.

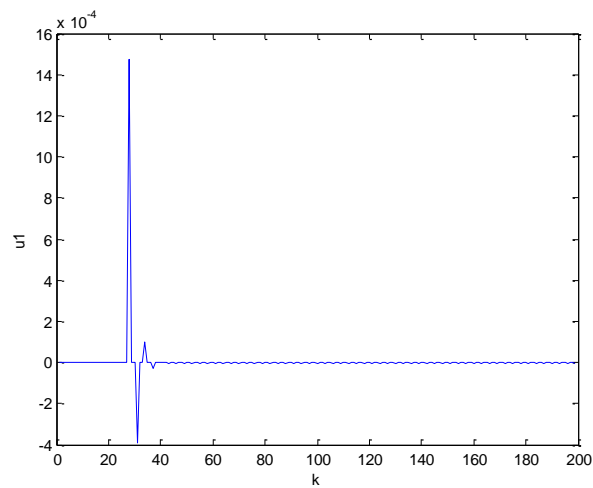


Fig. 5

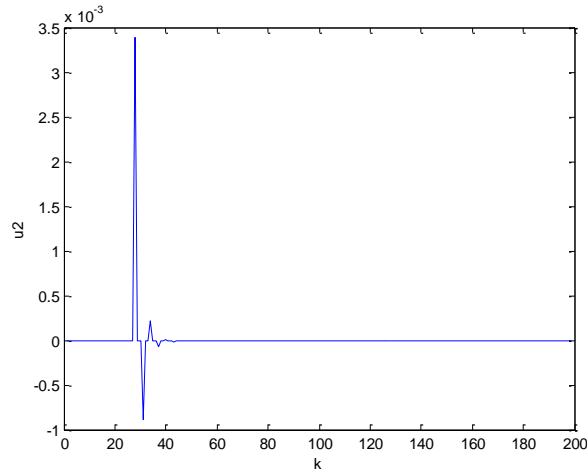


Fig. 6

Figs.5 and 6 show behaviors of the input controls u_1 and u_2 , respectively. These figures show that System (10) is stabilized by controller proposed in this paper.

5. Conclusions

In this paper, a new method based on Kannan mappings for chaotic synchronization is proposed. Furthermore, a new method based on the mappings is presented to stabilize chaotic discrete systems. These methods are applied to synchronize and control of chaotic discrete neural networks. Finally, a numerical example is given to validate the methods presented.

References

1. L. M. Pecora and L. Carroll. Synchronization in Chaotic Systems, *Physical Review Letters*, vol. 64, 821-824, 1990.
2. T. Ushio. Chaotic Synchronization and Controlling Chaos Based on Contraction Mappings, *Physics Letters A*, vol. 198, 14-22, 1995.
3. L. Liao and N. S. Huang. Control and Synchronization of Discrete Time Chaotic Systems via Variable Structure Control Technique, *Physics Letters A*, vol. 234, 262-268, 1997.
4. C. Yang, Z. Ge, C. Chang, and S. Li. Chaos Synchronization and Chaos Control of Quantum-CNN Chaotic System by Variable Structure Control and Impulse Control, *Nonlinear Analysis, Real World Applications*, vol. 11, 1977-1985, 2010.
5. D. Vassiliadis. Parametric Adaptive Control and Parameter Identification of Low Dimensional Chaotic Systems, *Physica D: Nonlinear Phenomena*, vol. 71, 319-341, 1994.
6. S. Chen and J. Lu. Parameters Identification and Synchronization of Chaotic Systems



- Based upon Adaptive Control, *Physics Letters A*, vol. 299, 353-358, 2002.
7. E. Solak, O. Morgul, and U. Ersoy. Observer-Based Control of A Class of Chaotic Systems, *Physics Letters A*, vol. 279, 47-55, 2001.
 8. J. A. Ramirez, H. Puebla, and I. Cervantes. Convergence Rate of Observer-Based Approach for Chaotic Synchronization, *Physics Letters A*, vol. 289, 193-198, 2001.
 9. L. Huang, R. Feng, and W. Wang. Synchronization of Chaotic Systems via Nonlinear Control, *Physics Letters A*, vol. 320, 271-275, 2004.
 10. J. H. Park. Chaos Synchronization of A Chaotic System via Nonlinear Control, *Chaos, Solitons, and Fractals*, vol. 25, 579-584, 2005.
 11. H. K. Chen. Global Chaos Synchronization of New Chaotic Systems via Nonlinear Control, *Chaos, Solitons, and Fractals*, vol. 23, 1245-1251, 2005.
 12. R. Tang and J. Xue. Chaotic Synchronization by Replacing Nonlinear Terms with Signals, *Chaos, Solitons, and Fractals*, vol. 28, 228-235, 2006.
 13. Z. Ge and P. Tsen. Two Theorems of Generalized Unsynchronization for Coupled Chaotic Systems, *Nonlinear Analysis, Theory, Method, and Applications*, vol. 69, 4230-4240, 2008.
 14. H. N. Agiza and M. T. Yassen. Synchronization of Rossler and Chen Chaotic Dynamical Systems Using Active Control, *Physics Letters A*, vol. 278, 191-197, 2001.
 15. M. T. Yassen. Chaos Synchronization Between Two Different Chaotic Systems Using Active Control, *Chaos, Solitons, and Fractals*, vol. 23, 131-140, 2005.
 16. E. Ott, C. Grebogi, and J. A. Yorke. Controlling Chaos, *Physical Review Letters*, vol. 64, 1190-1199, 1990.
 17. M. Kopel. Improving The Performance of An Economic System: Controlling Chaos, *Evolutionary Economics*, vol. 7, 269—289, 1997.
 18. L. Kass. Stabilizing Chaos in A Dynamical Macroeconomic Model, *Economic Behavior and Organization*, vol. 33, 313-332, 1998.
 19. J. A. Holyst and K. Urbanowicz. Chaos Control in Economical Model by Time-Delayed Feedback Method, *Physica A*, vol. 287, 587-598, 2000.
 20. H. Yu, Y. Liu, and J. Peng. Control of Chaotic Neural Networks Based on Contraction Mappings, *Chaos, Solitons, and Fractals*, vol. 22, 787-792, 2004.
 21. K. Aihara, T. Takabe, and M. Toyoda. Chaotic Neural Network, *Physics Letters A*, vol. 144, 333-340, 1990.
 22. S. Nara, P. Davis, and H. Totsuji. Memory Search Using Complex Dynamics in A Recurrent Neural Network Model, *Neural Networks*, vol. 6, 963-973, 1993.
 23. R. Sole, L. Menendez, and D. Prida. Controlling Chaos in Discrete Neural Networks, *Physics Letters A*, vol. 199, 65-69, 1995.
 24. H. Sabbagh. Control of Chaotic Solutions of The Hindmarsh-Rose Equations, *Chaos, Soliton, and Fractals*, vol. 112, 1213-1218, 2000.
 25. R. Kannan. Some Results on Fixed Points-II, *American Mathematical Monthly*, vol. 76, 405-408, 1969.
 26. T. Shinbrot, C. Grebogi, E. Ott, and J. York. Using Small Perturbations to Control Chaos, *Nature*, vol. 363, 411-417, 1993.



On the Computation of the Kantorovich Distance for Images

Constantinos Alexopoulos¹ and Vassileios Drakopoulos²

¹ University of Athens, Panepistimioupolis, 15784 Athens, Greece
(E-mail: calexop@di.uoa.gr)

² University of Athens, Panepistimioupolis, 15784 Athens, Greece
(E-mail: vasilios@di.uoa.gr)

Abstract. We consider the theory and applications of the Kantorovich metric in fractal image compression. After surveying the most important approaches for its computation, we highlight its usefulness as a mathematical tool for comparing two images and improve its performance by means of more appropriate data structures.

Keywords: Fractals, Hutchinson metric, Image comparison, Kantorovich metric.

1 Introduction

In many fields of computer science like pattern recognition and image processing, it is important to have an efficient way to compare geometric objects. The natural approach to this problem is to define a metric in the space of the geometric objects and use this metric to compute the distance between them. Considering digitized images as geometric objects, we can use that metric to compare them.

The *Kantorovich* (or *Hutchinson*) *metric*, a.k.a. Wasserstein (or Vaserstein), earth mover's or match metric, takes into account the spatial structure of the compared images and, hence, corresponds more closely than other metrics to our notion of the visual differences between two images. John E. Hutchinson[6] used the Kantorovich distance to measure the distance between self-similar probability measures obtained as limiting distributions for a fairly simple type of Markov chains induced by affine, contractive mappings. He used the Kantorovich metric to prove an existence and uniqueness theorem of such limit measures.

The Kantorovich metric is also used by Michael F. Barnsley[2] and co-workers to approach the convergence of *iterated function systems*, which were introduced by Hutchinson. In trying to solve the so-called “inverse problem” or “image encoding problem”, i.e. find an IFS that generates a predetermined image, it is natural to use this metric as an objective function to be minimised. Moreover, this metric appears to be a good indicator of the perceived difference between two images.

Considering digitized images as a set of pixels, the problem of computing the Kantorovich distance between them is equivalent to the formulation of a *linear programming problem* called the *balanced transportation problem*.



According to Michael Werman *et al.*[9] the computational complexity of standard algorithms for transportation problems are of order $O(N^3)$, where N denotes the total number of pixels in the compared images. An algorithm for the computation of the Hutchinson metric in the case of finite one-dimensional sequences is presented in [3].

Thomas Kaijser[7] presented a variation of the primal-dual algorithm for computing the Kantorovich distance function. To decrease the computational complexity for updating the values of the dual variables for both transmitting and receiving images, he always increases them by a constant value of 1. Unfortunately, this is applicable, only if the underlying pixel distance value is the L_1 -metric. Moreover, he developed two methods for fast determination of new admissible arcs, one for the L_1 -metric and one for the L_2 -metric. Kaijser's method was implemented by Niclas Wadströmer[8] in the context of his PhD thesis, but the data structures used to implement the above mentioned method as well as the way that the labelling procedure was implemented are not so clear.

Another work on the computation of the Kantorovich distance is the one of Drakopoulos V. *et al.*[5]. In this work the problem of computing the Kantorovich distance is transformed into a linear programming problem which is solved using the simplex method. To decrease the computational complexity of the method, they developed an approximation algorithm for "large images". Yuxin Deng *et al.*[4] give a brief survey of the applications of the Kantorovich distance in probabilistic concurrency, image retrieval, data mining and bioinformatics.

The main purpose of the present paper is to improve the algorithm presented by Thomas Kaijser for computing the Kantorovich distance function by means of more appropriate data structures. The metric we are using as the underlying distance-function between pixels is the L_1 -metric. Using kd -trees we don't have to use different methods, but only to change the metric for the construction of the appropriate kd -tree.

2 Problem formulation

We are interested in computing the *Kantorovich distance* between grey-scale images. There are three types of image models: Measure spaces, pixelated data and functions. Using this approach, we consider an image as a measure space. Therefore, by an image P with support K we mean an *integer-valued* nonnegative function $p(i, j)$ defined on K , i.e. $P = \{p(i, j) : (i, j) \in K\}$. We define as a *Borel measure* on the space of grey-scale images the *pixel value* $p(i, j)$, where i and j are the Cartesian coordinates of the pixel.

For a compact metric space (X, d) , let P_1 and P_2 be two Borel probability measures on X and define $\Theta(P_1, P_2)$ as the set of all probability measures P on $X \times X$ with *fixed marginals* $P_1(\cdot) = P(\cdot \times X)$ and $P_2(\cdot) = P(X \times \cdot)$. Next,



let

$$\text{Lip}(X) = \{f: X \rightarrow \mathbb{R} \mid |f(x) - f(y)| \leq d(x, y), \forall x, y \in X\}$$

and define the distance between P_1 and P_2 as

$$B_d(P_1, P_2) = \sup \left\{ \left| \int_X f(x) P_1(dx) - \int_X f(x) P_2(dx) \right|, f \in \text{Lip}(X) \right\}.$$

The images considered are sets of finite collection of pixels, so they constitute compact metric spaces.

Let K_1 and K_2 be two images, S_n , $1 \leq n \leq N$ be the pixels of K_1 and R_m , $1 \leq m \leq M$ the pixels of K_2 . Using the terminology of Kaijser we call K_1 the *transmitting image* and K_2 the *receiving image*; S_n , $1 \leq n \leq N$ denote *sources* whereas R_m , $1 \leq m \leq M$ denote *sinks* or *destinations*. By a *flow* we mean the amount of goods sent from the source S_n to the sink R_m denoted by $x(n, m)$ whereas $c(n, m)$, $1 \leq n \leq N$, $1 \leq m \leq M$ denote the cost of transferring goods from S_n to R_m . In our case the cost corresponds to the distance between S_n and R_m . If $a(n)$ denote the amount of goods available in a source and $b(m)$ the amount of goods needed in a sink, the Kantorovich distance between K_1 and K_2 can be formulated as a balanced transportation problem as follows:

$$\text{Minimize } \sum_{n=1}^N \sum_{m=1}^M c(n, m) \cdot x(n, m)$$

subject to $x(n, m) \geq 0$, $1 \leq n \leq N$, $1 \leq m \leq M$,

$$\sum_{m=1}^M x(n, m) = a(n), \quad 1 \leq n \leq N \quad (1)$$

$$\sum_{n=1}^N x(n, m) = b(m), \quad 1 \leq m \leq M \quad (2)$$

and

$$\sum_{n=1}^N a(n) = \sum_{m=1}^M b(m).$$

The distance can be any of the following distances: L_1 -metric or L_2 -metric. For each source and each sink we define two quantities $\alpha(n)$ and $\beta(m)$ respectively, called *dual variables*. If

$$c(n, m) - \alpha(n) - \beta(m) \geq 0, \quad 1 \leq n \leq N, 1 \leq m \leq M,$$

we call the set of dual variables *feasible*. A pair of indices (n, m) , where n is an index of a source S_n and m is an index of a sink R_m , is called an *arc*. If an arc (n, m) satisfies the condition

$$c(n, m) - \alpha(n) - \beta(m) = 0, \quad (3)$$



where $d(n, m)$ is the underlying distance-function between the pixels S_n and R_m , it is called an *admissible arc*; otherwise it is called *nonadmissible*. We say that a flow is *optimal* if Equations (2) and (3) hold.

The dual version of the transportation problem is

$$d_K(P, Q) = \text{Max} \left\{ \sum_{n=1}^N \alpha(n) \cdot a(n) + \sum_{m=1}^M \beta(m) \cdot b(m) \right\} \quad (4)$$

when the set of dual variables is feasible.

3 The proposed algorithm

Our algorithm is based on the well known *primal-dual algorithm* which solves the balanced transportation problem on the plane. We make several enhancements, however, that improve the efficiency of the algorithm. Our improvements are based on the data structures used to store image data and on the fact that the transportation cost is the distance between the pixels. The latter allows us to use some spatial data structures which facilitate the computations and minimise the complexity of the problem. Before describing our method in detail, we give the main steps of the primal-dual algorithm:

1. Determine an initial value of the dual variables, find the corresponding set of admissible arcs and their flow.
2. Check if the current admissible flow is maximal. If it is go to (4), else go to (3).
3. Update the admissible flow and go to (2).
4. Check if the current maximal flow is optimal. If it is go to (7), else go to (5).
5. Update the dual variables.
6. Find the new admissible arcs and go to (2).
7. Stop.

Let us define as *total transporting grey mass* the summation of the grey value of all pixels in the transporting image. Similarly, we define as *total receiving grey mass* the summation of the grey value of all pixels in the receiving image. In order to convert the Kantorovich distance problem between images to a balanced transportation problem on the plane, both transporting and receiving total grey values must be equal. In general, these two amounts are different and in order to make them equal we change both masses accordingly applying the following formula on every single pixel value of both images:

$$p_{new}(n) = p(n) \cdot \hat{L}(K_2), \quad \hat{L}(K_2) = \left(\sum_{m=1}^M q(m) \right) / GCD(L, Q),$$

$$q_{new}(m) = q(m) \cdot \hat{L}(K_1), \quad \hat{L}(K_1) = \left(\sum_{n=1}^N p(n) \right) / GCD(L, Q),$$



where $p(n)$ and $q(m)$ are the pixel values of the transmitting and receiving images respectively, $L = \sum_{n=1}^N p(n)$, $Q = \sum_{m=1}^M q(m)$ and $GCD(L, Q)$ is the greatest common divisor of L and Q . In the following we shall describe our algorithm as well as the data structures we use to facilitate our computations and image storage.

3.1 Dual variables and the flow of the current admissible arcs

After having made the total grey masses of both images equal we have to initialise the dual variables. We set as initial values $\alpha(n) = \min\{d(n, m), 1 \leq m \leq M\}$, $i \leq n \leq N$ and $\beta(m) = 0$, $1 \leq m \leq M$. From the above equations we observe that the initial values of the dual variables $\alpha(n)$ associated with the transmitting image pixels, are the distances of their nearest neighbour pixels of the receiving image. In order to compute this quantity we create a *kd-tree* structure¹ using the coordinates of the receiving image pixels and we search for the nearest neighbour of every single transmitting pixel. So, if n is a transmitting pixel and m one of its nearest neighbours in the receiving image, then (n, m) is an admissible arc. Therefore, the initial flow along this arc is $x(n, m) = \min\{p(n), q(m)\}$, whereas the new pixel values are $p(n) - x(n, m)$ and $q(m) - x(n, m)$.

3.2 Increasing the flow along the current set of admissible arcs

We call *surplus source* a transmitting pixel with $p(n) > 0$; otherwise, it is called a *zero source*. A receiving pixel having $q(m) > 0$ is called a *deficient sink*; otherwise, it is called *zero sink*. We define as *augmenting path* a set of admissible arcs connecting sources and sinks starting from a surplus source and ending with a deficient sink running through zero sinks and sources interchangeably. Moreover, the flow along admissible arcs connecting zero sinks with zero sources must be positive. In this step we use a labelling procedure to determine augmenting paths. It is clear that we can have flow increment only along augmenting paths. The labelling procedure is described as follows.

Start by labelling all surplus sources and then label all sinks that are connected to those sources with admissible arcs. Then, using the last labelled sinks, label all sources that are not labelled yet and are connected to those sinks with admissible arcs of positive flow. Repeat the above procedure until either a deficient sink is labelled or no more nodes can be labelled. If a deficient sink is labelled, then proceed to flow augmentation along the path that has been found. If no such path is found, the current admissible flow is maximal. For faster labelling procedure, we don't use any extra data structure. We reorder the pixels of both the transmitting and the receiving image in the initial data structure depending on whether they are labelled

¹ <http://www.cs.umd.edu/~mount/ANN/>



or unlabelled. To speed up the reordering process, we store the pixel data in doubly linked lists which need $O(1)$ to move the nodes along the list.

Let $\theta_1 = \min\{x(m, n)\}$ be the minimum value of the positive flows belonging to the augmenting path connecting a labelled source and a label sink directed from sink to source. We define by

$$\theta = \min \left\{ a(n) - \sum_{j=1}^M x(n, j), b(m) - \sum_{i=1}^N x(i, m), \theta_1 \right\}.$$

Then, we can increase the flow along the path by setting the value of the starting source pixel to $p(n) - \theta$, the value of the ending sink to $q(m) - \theta$, by increasing the flows directed from source to sink by θ and by decreasing the flows from sink to source by the same amount. A drawback of this labelling procedure is that, after increasing the flow along an augmenting path, we may obtain *cycles*. In order to avoid them, we change the way we apply the labelling procedure by using only positive admissible arcs during the whole procedure. In that way, however, we cannot find all the augmenting paths. So, we use a *flow tuning procedure* which finds all possible augmenting paths for the current set of admissible arcs without having to store and use all the zero flow admissible arcs.

3.3 Flow tuning procedure

We define as *surplus flow tree* a set of paths starting from a surplus source and ending to zero sinks. A *zero flow tree* is a flow tree with a zero source as starting node. The main purpose of the flow tuning procedure is to find admissible arcs that connect zero sources belonging to surplus flow trees and unlabelled deficient sinks. To do that, a *kd-tree* is constructed using the coordinates of the unlabelled deficient sinks. Then, using the *kd-tree* structure for each zero source belonging to a surplus flow tree, we locate all the deficient unlabelled sinks that lay within a distance $\alpha(n)$ from itself. After that, a new augmenting path has been located and the flow is augmented as described in the previous subsection. According to the definition of the augmenting path, there is no reason to search for arcs that connect zero sources that belong to zero flow trees with unlabelled zero sinks. In such a way we decrease the number of sinks as well as the number of considered sources. The first one leads to a faster construction of the *kd-tree* whereas the second one minimises the number of input points.

3.4 Dual variable update and the new set of admissible arcs

When no more augmenting paths can be located for the current set of admissible arcs, we proceed to the dual variable update procedure. The main reason for updating the dual variables associated with both sources and sinks



is to create new admissible arcs in order to achieve the maximal and also the optimal flow. According to Kaijser[7], if the underlying metric is the L_1 -metric, the dual variable can be changed by $\delta = 1$. In order to preserve the current flow along the current set of admissible arcs, the dual variables are changed as follows:

$$\begin{aligned}\alpha_{new}(n) &= \alpha_{old}(n) + \delta, & n \in M_1, & \quad \alpha_{new}(n) = \alpha_{old}(n), & n \in U_1, \\ \beta_{new}(m) &= \beta_{old}(m) - \delta, & m \in M_2, & \quad \beta_{new}(m) = \beta_{old}(m), & m \in U_2,\end{aligned}$$

where M_1 and M_2 denote the sets of indices of labelled sources and sinks, respectively, whereas U_1 and U_2 denote the sets of indices of unlabelled sources and sinks, respectively. To improve the dual variable update, we define a new variable Δ as the running total of the dual variable changes as the algorithm evolves; see also [1]. We apply the above mentioned dual variable change routine using Δ instead of δ . Because of the way we change the dual variables, new positive flow admissible arcs are created between the labelled surplus sources and the unlabelled deficient sinks. To find out the new set of admissible arcs, a kd -tree is constructed using the coordinates of the unlabelled deficient sinks. Then, for each surplus source, we locate all the deficient sinks that lay within a distance of $\alpha(n) + \Delta$ from it. After finding out the new set of positive flow admissible arcs, the algorithm is applied again until no more surplus nodes exist.

4 Results

We now present typical results from the application of our algorithm to real images, aiming to demonstrate its applicability to the demanding problems inherent in the image compression area and its performance. The original images used as our reference point in the experiments presented here are the $256 \times 256 \times 8$ bpp Lena and Barbara images shown in Figure 1. We examine for each original image how close it is to a filtered or compressed replica of it. In other words we seek to measure the difference (i.e. the error) between two images by computing the Kantorovich distance between the original image and each of the associated filtered ones.

	μ, μ_1	μ, μ_2	μ, μ_3	ν, ν_1	ν, ν_2	μ, ν
d_K	2,789,456	8,562,357	4,532,730	3,125,789	8,998,678	15,853,930
t_K	27:26	42:22	41:15	31:52	44:27	1:12:36

Table 1. The Kantorovich distance d_K between the real-world images and the computation time in hour:min:sec format.

The correspondence between the images of Lena and the indices is the following: μ = original image, μ_1 = wavelet compression, μ_2 = JPEG compression and μ_3 = 8:1 fractal compression. The correspondence between the



Fig. 1. The original images of Lena (left) and Barbara (right) used in our experiments ($256 \times 256 \times 8$ bpp).

images of Barbara and the indices is the following: ν = original image, ν_1 = 64:1 compression and ν_2 = JPEG compression. Time results are given in CPU minutes on a CoreTM 2 Duo PC with a 2.13 GHz CPU clock, 4 GB RAM and running Windows 7 Ultimate. Looking at Table 1 from left to right we can see, which of the images are closer to the originals. The runtime of our algorithm is better than the one presented in [7].

References

- 1.D.S. Atkinson and P.M. Vaidya. Using geometry to solve the transportation problem in the plane. *Algorithmica*, 13:442461, 1995.
- 2.M.F. Barnsley. *Fractals everywhere*, 2nd ed., San Diego, 1993. Academic Press Professional.
- 3.J. Brandt, C. Cabrelli and U. Molter. An algorithm for the computation of the Hutchinson distance. *Information Processing Letters*, 40:113–117, 1991.
- 4.Y. Deng and W. Du. The Kantorovich metric in Computer Science: A brief survey. *Electronic Notes in Theoretical Computer Science*, 253:73–82, 2009.
- 5.V. Drakopoulos and N. P. Nikolaou. Efficient computation of the Hutchinson metric between digitized images. *IEEE Transactions on Image Processing*, 13:1581–1588, 2004.
- 6.J.E. Hutchinson. Fractals and self similarity. *Indiana University Mathematics Journal*, 30: 713–747, 1981.
- 7.T. Kaijser. Computing the Kantorovich distance for images. *Journal of Mathematical Imaging and Vision*, 9:173–191, 1998.
- 8.N. Wadströmer. Coding of fractal binary images with contractive set mappings composed of affine transformations, *PhD thesis*, Linköping University, 2001.
- 9.M. Werman, S. Peleg and A. Rosenfeld. A distance metric for multidimensional histograms. *Computer Vision Graphics Image Processing*, 32:328–336, 1985.



Routes to chaos in confined thermal convection arising from a cylindrical heat source

Diego Angeli¹, Arturo Pagano²,
Mauro A. Corticelli¹, and Giovanni S. Barozzi¹

¹ University of Modena and Reggio Emilia, Department of Mechanical and Civil Engineering, Via Vignolese, 905, I-41125 Modena, Italy

(E-mail: diego.angeli@unimore.it)

² University of Catania, Department of Industrial and Mechanical Engineering Viale Andrea Doria, 6, I-95125 Catania, Italy

(E-mail: apagano@diim.unict.it)

Abstract. Natural convection flows arising from a horizontal cylinder centred in a square-sectioned enclosure are studied numerically. The sequence of bifurcations marking the transition of base fixed-point solutions to unsteady, chaotic flows is followed for increasing values of the Rayleigh number, and for two values of the enclosure aspect ratio, A . It is observed that, for the lower A -value, the route to chaos is triggered by a supercritical Hopf bifurcation, followed by a sequence of period-doublings, while, for the higher A -value, the symmetry of the system is broken by a pitchfork bifurcation, with periodic orbits originating from both branches, and eventually approaching chaos, exhibiting features typical of blue-sky catastrophes.

Keywords: Thermal convection, transition to chaos, bifurcations, period-doubling.

1 Introduction

Buoyancy-induced flows in enclosures are very complex in nature, and highly unpredictable, due to the bi-directional interaction between the flow and temperature fields, and the sensitivity of the thermal-flow regimes to the geometric and thermal configuration of the system.

The importance of bifurcations and chaos in buoyancy-induced flows as a research topic goes far beyond the field of thermal sciences. In fact, it is deeply entwined with the history of chaos theory, since the discovery of the renown Lorenz attractor, originating from a simplified Rayleigh-Bénard convection model [1]. From that seminal study, many works have been carried out on the non-linear dynamics of thermal convection in basic enclosure configurations, such as the rectangular enclosures heated from below and from the side [2,3], and, more recently, the horizontal annulus between two coaxial cylinders [4]. Fewer works dealt with more complex geometrical and thermal configurations [5,6]. Nevertheless, from a theoretical and practical standpoint, the interest in this topic is growing continuously.

The physical system considered in the present study is the cavity formed by an infinite square parallelepiped with a centrally placed cylindrical heating

source. The system is approximated to its 2D transversal square section containing a circular heat source, as sketched in Fig. 1. The temperature of both enclosure and cylinder is assumed as uniform, the cylindrical surface being hotter than the cavity walls. The resulting flow is investigated with respect to the leading parameter of the non-dimensionalized problem, the Rayleigh number Ra , based on the gap width H , and for two values of the aspect ratio $A = L/H$, between the cavity side length and the minimum enclosure to cylinder gap width, namely $A = 2.5$ and $A = 5$. The third parameter of the system, the Prandtl number, is fixed at a value $Pr = 0.7$, representative of air at environmental conditions.

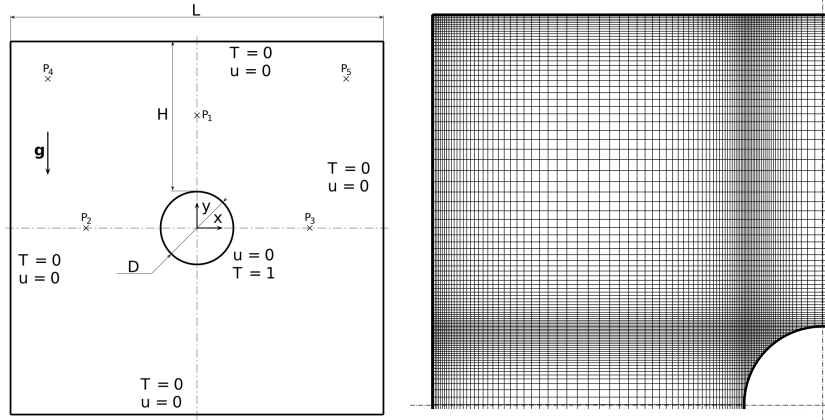


Fig. 1. Left: schematic of the system under consideration; (x) symbols indicate locations of the sampling points. Right: quadrant of the computational grid for $A = 2.5$.

Numerical predictions are carried out by means of a specifically developed finite-volume code. Successive bifurcations of the low- Ra fixed point solution are followed for increasing Ra . To this aim, time series of the dependent variables (velocity components and temperature), are extracted in 5 locations represented in Fig. 1 by points P_1 to P_5 . Nonlinear dynamical features are described by means of phase-space representations, power spectra of the computed time series, and of Poincaré maps.

2 Numerical method

The problem is stated in terms of the incompressible Navier-Stokes formulation, under the Boussinesq approximation. The governing equations (continuity, momentum and energy) are tackled in their non-dimensional form:



$$\nabla \cdot \mathbf{u} = 0 \quad (1)$$

$$\frac{\partial \mathbf{u}}{\partial t} + \mathbf{u} \cdot \nabla \mathbf{u} = -\nabla p + \frac{Pr^{1/2}}{Ra^{1/2}} \nabla^2 \mathbf{u} + T \hat{\mathbf{g}} \quad (2)$$

$$\frac{\partial T}{\partial t} + \mathbf{u} \cdot \nabla T = \frac{1}{(RaPr)^{1/2}} \nabla^2 T \quad (3)$$

where t , \mathbf{u} , p and T represent the dimensionless time, velocity vector, pressure and temperature, respectively, and $\hat{\mathbf{g}}$ is the gravity unit vector. A value $Pr = 0.7$ is assumed for air. Boundary conditions for T and \mathbf{u} are reported in Figure 1.

The numerical technique adopted is based on a second-order, Finite Volume implementation of equations (1)-(3) on non-uniform Cartesian grids: a more detailed description of the spatial and temporal discretization schemes is found in [7]. The 2D modelling of arbitrarily irregular boundaries on Cartesian grids is achieved thanks to the original scheme developed by Barozzi *et al.* [8], which preserves second-order accuracy for the method, as well as the computational efficiency of the Cartesian approach.

In view of the work objectives, special care was put on the grid sizing of both near-wall areas and internal domain regions, as shown in Fig. 1. The average cell spacing in each region was chosen according to scaling considerations, as illustrated in [6]. The time step size has been chosen small enough so as to ensure a suitably accurate reproduction of the continuous-time system dynamics.

For either A -value, the initial conditions were chosen so as to follow the evolution of low- Ra base-flow, fixed-point solutions [7]. In order to detect the occurrence of successive bifurcations, Ra was increased monotonically with suitable steps, each simulation starting from the final frame of the preceeding one. All the simulations were protracted to steady-state or, when unsteady flows were detected, until a fixed dimensionless time span was covered.

$A = 2.5$ (190×190 grid)		$A = 5$ (288×288 grid)	
Ra	Bifurcation	Ra	Bifurcation
4×10^4	S (base flow)	1.8×10^4	S (base flow)
$6.6 \sim 6.8 \times 10^4$	$S \rightarrow P_1$ (supercritical Hopf)	$3.2 \sim 3.4 \times 10^4$	$S \rightarrow NS$ (pitchfork)
$1.7 \sim 1.8 \times 10^5$	$P_1 \rightarrow P_2$ (period-doubling)	$6.0 \sim 7.0 \times 10^4$	$NS \rightarrow P$ (Hopf)
$1.8 \sim 1.9 \times 10^5$	$P_2 \rightarrow P_4$ (period-doubling)	$6.0 \sim 7.0 \times 10^5$	$P \rightarrow N$ (Blue-sky catastrophe)
$1.9 \sim 2.0 \times 10^5$	$P_4 \rightarrow \dots \rightarrow N$		

Table 1. Bifurcations of the low- Ra base flow solution for each A .



3 Results and discussion

Table 2 summarizes the sequences of bifurcations leading to chaos for both values of the aspect ratio A . The nomenclature used in defining the different types of asymptotic behaviours follows the systematic introduced by Angeli *et al.* [4]. In the following, details of both routes are briefly illustrated by means of established nonlinear analysis tools.

For $A = 2.5$, starting from the base solution at $Ra = 4 \cdot 10^4$, the system asymptotically reaches a fixed-point for $Ra \leq 6.6 \times 10^4$. As Ra is increased from $Ra = 6.6 \times 10^4$ to $Ra = 6.8 \times 10^4$, oscillatory behaviour sets in, until a periodic limit cycle is reached. In Fig. 2, 2D projections of the corresponding T - u_x - u_y attractors are plotted as a function of Ra . The passage from the lower- Ra fixed-point solution to the periodic orbit is clearly portrayed, thus suggesting the occurrence of a Supercritical Hopf bifurcation.

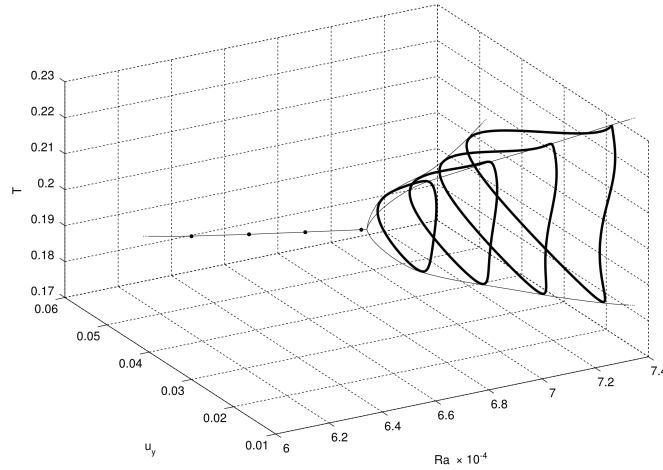


Fig. 2. Sequence of 2D attractors u_y - T at point P2, for $A = 2.5$ and for increasing Ra .

Fig. 3 reports the power spectral density distribution of the temperature time series at point P1 for the case $A = 2.5$ and for increasing values of the Rayleigh number. The values of Ra have been chosen with the aim of showing the occurrence of a period doubling route to chaos which characterises the evolution of the system dynamics for the mentioned aspect ratio. In fact, it is possible to observe that the two original fundamental harmonics observed in the power spectrum of temperature at $Ra = 1.7 \times 10^5$ become four for $Ra = 1.8 \times 10^5$ and double again for $Ra = 1.9 \times 10^5$; the last case, at $Ra = 2.0 \times 10^5$, is instead characterised by a broadband power spectrum,



which represents a first hint of chaotic dynamics, with the broadened bands arising around the original harmonics of the previous cases.

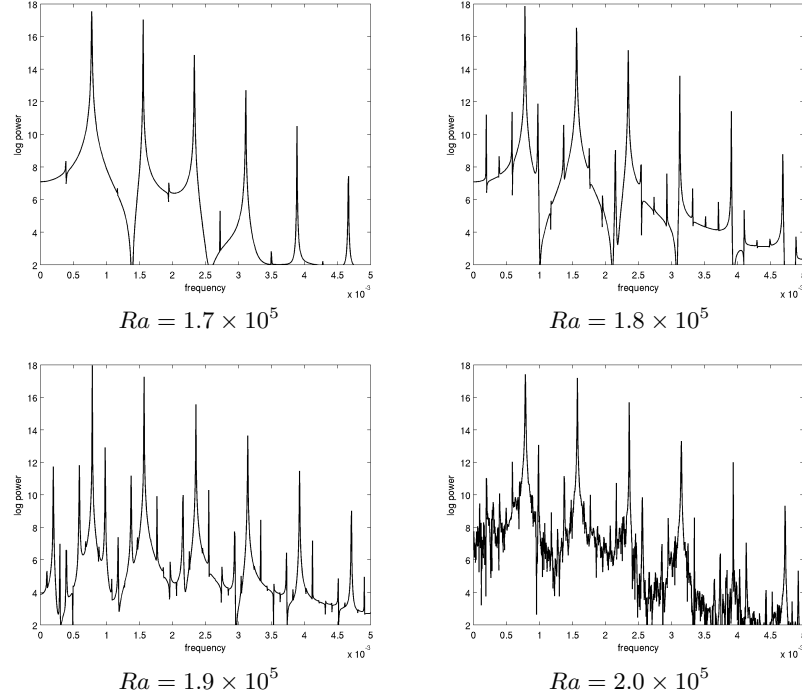


Fig. 3. Power spectral density of T at point P1, for $A = 2.5$ and for increasing Ra

This observation is confirmed by the analysis of the system attractors reported in the T - u_x - u_y state space, as reported in Fig. 4. Considering that each of the fundamental harmonics observed in the power spectrum corresponds to a loop of the attractor in the phase space representation, it is possible to observe that the original two-loop limit cycle at $Ra = 1.7 \times 10^5$ gives rise to a four-loop limit cycle at $Ra = 1.8 \times 10^5$, which, in turn, is doubled again in a eight-loop limit cycle at $Ra = 1.9 \times 10^5$. Finally, for the last of the reported values of Ra , $Ra = 2.0 \times 10^5$, in accordance with previous observations on the power spectrum, the attractor shows a chaotic morphology, with fractal bands distributed around the loops of the original limit cycles.

Fig. 4 reports also the intersections of the 3-dimensional attractors with Poincaré surfaces of section that have been obtained considering the plane u_x - T passing by the mean values of the calculated time series of the state variable u_y . Such intersections have been reported in the maps in Fig. 5. It is observed that a couple of intersections arises for each loop of the limit cycle. Again,

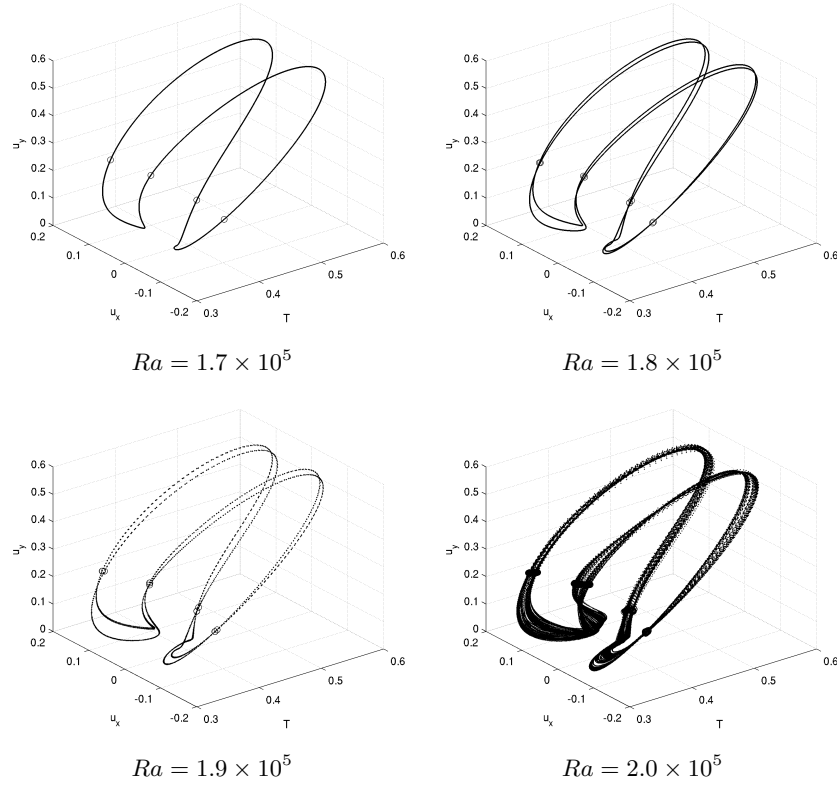


Fig. 4. 3D attractor in state space T - u_x - u_y at point P1, for $A = 2.5$ and for increasing Ra

the successive period doublings can be observed by spanning the maps at $Ra = 1.7 \times 10^5$ to $Ra = 1.8 \times 10^5$ and, then, to $Ra = 1.9 \times 10^5$, whereas ordered series of intersections, typical of deterministic chaotic dynamics, characterise the Poincaré map at $Ra = 2.0 \times 10^5$. For brevity, it is just mentioned here that an accurate observation of the local structure of such series of intersections reveals the stretching and folding typical of fractal sets.

For the higher value of the aspect ratio A considered, $A = 5$, the system undergoes a different sequence of bifurcations leading to chaos. Fig. 6(a) represents the evolution of the T - u_y attractors at point P2 as a function of Ra . As Ra is increased beyond $Ra = 3.2 \times 10^4$, the base flow becomes unstable, and gives rise to two different solution branches, suggesting the occurrence of a pitchfork bifurcation (whose sub- or supercritical nature is still to be ascertained). The two solution branches correspond to stable mirrored dual solutions [6].

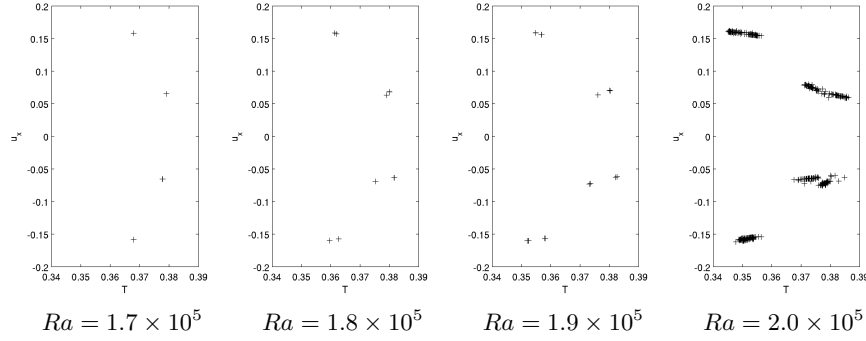


Fig. 5. Poincaré surfaces of section of the 3D attractors at point P1, for $A = 2.5$ and for increasing Ra

By further increasing Ra , each of the two solution branches undergo a Hopf bifurcation to a periodic limit cycle, as clearly visible in Fig. 6(a). Such transition occurs between $Ra = 6 \times 10^4$ and $Ra = 7 \times 10^4$. The periodic orbits remain stable for a wide range of Ra -values, up to $Ra = 6 \times 10^5$. From Fig. 6(b), a progressive increase of the period of the limit cycle, *i.e.* of the loop extension can be appreciated. This trend eventually leads to the chaotic attractor reported in Fig. 6(c), for $Ra = 7 \times 10^5$, in a general evolution which seems to belong to the class of blue-sky catastrophes [9]. Such an observation deserves further analyses which, however, are beyond the scope of the present study.

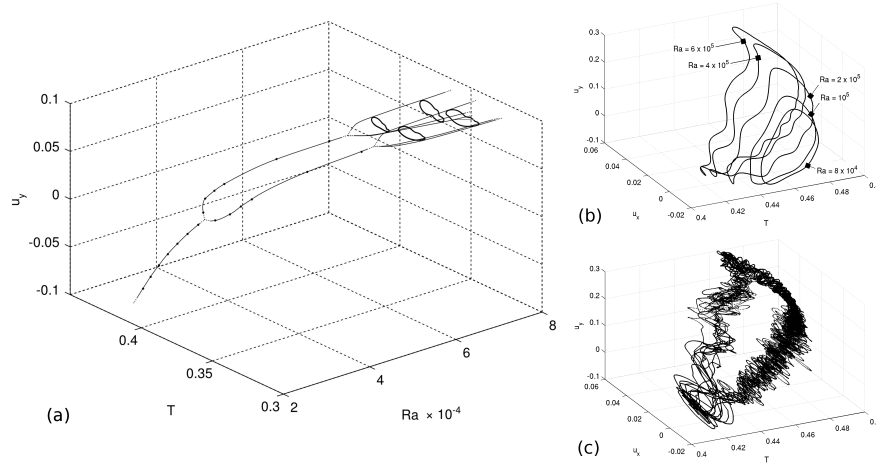


Fig. 6. (a) Sequence of 2D attractors $T-u_y$ at point P2, for $A = 5$ and for increasing Ra ; (b) 3D periodic orbits in state space $T-u_x-u_y$ at point P1, for $A = 5$ and for increasing Ra ; (c) chaotic attractor at point P1, for $A = 5$ and $Ra = 7 \times 10^5$.



4 Concluding remarks

Natural convection flows arising from a horizontal cylindrical source centred in a square enclosure were investigated numerically. Two values of the aspect ratio A were considered; for which the entire scenario leading to deterministic chaos was outlined, for increasing values of the Rayleigh number.

For the lower A -value, $A = 2.5$, the flow undergoes a Hopf bifurcation, followed by a sequence of period-doublings. For the higher A -value, $A = 5$, a pitchfork bifurcation gives rise to stable periodic orbits, persisting for a large range of Ra -values. Chaotic behaviour is finally observed, on top of an evolution which resembles a blue-sky catastrophe.

References

- 1.E. N. Lorenz. Deterministic nonperiodic flow. *Journal of Atmospheric Sciences*, 20:130–141, 1963.
- 2.K. T. Yang. Transitions and bifurcations in laminar buoyant flows in confined enclosures. *ASME Journal of Heat Transfer*, 110:1191–1204, 1988.
- 3.P. Le Quéré. Onset of unsteadiness, routes to chaos and simulations of chaotic flows in cavities heated from the side: a review of present status. In G. F. Hewitt, editor, *Proceedings of the Tenth International Heat Transfer Conference*, volume 1, pages 281–296, Brighton, UK, 1994. Hemisphere Publishing Corporation.
- 4.D. Angeli, G. S. Barozzi, M. W. Collins, and O. M. Kamiyo. A critical review of buoyancy-induced flow transitions in horizontal annuli. *International Journal of Thermal Sciences*, 49:2231–2492, 2010.
- 5.G. Desrayaud and G. Lauriat. Unsteady confined buoyant plumes. *Journal of Fluid Mechanics*, 252:617–646, 1998.
- 6.D. Angeli, A. Pagano, M. A. Corticelli, A. Fichera, and G. S. Barozzi. Bifurcations of natural convection flows from an enclosed cylindrical heat source. *Frontiers in Heat and Mass Transfer*, accepted for publication, 2011.
- 7.D. Angeli, P. Levoni, and G. S. Barozzi. Numerical predictions for stable buoyant regimes within a square cavity containing a heated horizontal cylinder. *International Journal of Heat and Mass Transfer*, 51:553–565, 2008.
- 8.G. S. Barozzi, C. Bussi, and M. A. Corticelli. A fast cartesian scheme for unsteady heat diffusion on irregular domains. *Numerical Heat Transfer B*, 46:56–77, 2004.
- 9.Y. Kuznetsov. *Elements of Applied Bifurcation Theory*, volume 112 of *Applied Mathematical Sciences*. Springer-Verlag, New York, 2nd edition, 1998.



On some $p(x)$ –quasilinear problem in non variational case

M. B. BENBOUBKER¹ and E. AZROUL¹

Faculty of Sciences Dhar-Mahraz Department of mathematics, B.P. 1796 Fs
Morocco (E-mail: azroulelhoussine@gmail.com, simo.ben@hotmail.com)

Abstract. We consider a class of nonlinear elliptic equations containing a $p(x)$ -Laplacian type operator, lower order terms having nonstandard growth. The model example is the equation

$$-\Delta_{p(x)}u + |u|^{p(x)-2}u = \mu$$

in a bounded set $\Omega \subset \mathbb{R}^N$, coupled with a Dirichlet boundary condition. For some right-hand side measure μ which admits some decomposition in $L^1(\Omega) + W^{-1,p'(x)}(\Omega)$.

Keywords: Nonlinear elliptic equation, Sobolev spaces with variable exponent, entropy strongly-regular solution, truncations..

1 Introduction

The study on problems of elliptic equations and variational problems with $p(x)$ -growth conditions has attracted more and more interest in the recent years. The aim of this paper is to discuss the existence of entropy strongly-regular solution of the following quasilinear $p(x)$ -Laplacian

$$\begin{cases} -\Delta_{p(x)}u + |u|^{p(x)-2}u = \mu & \text{in } \Omega \\ u = 0 & \text{on } \partial\Omega. \end{cases} \quad (1)$$

where $\mu \in L^1(\Omega) + (L^{p'(x)}(\Omega))^N$, and where Ω is a bounded open subset of \mathbb{R}^N ($N \geq 2$), $p \in C(\bar{\Omega})$, $p(x) > 1$. Especially, when $p(x) = p = \text{cte}$, (1) is the well known quasilinear p -Laplacian equation. There have been a large no. of papers on the existence of solutions for p -Laplacian equations. For the existence of solutions for $p(x)$ -Laplacian Dirichlet problems on a bounded domain we refer to [11,12].

The natural framework to solve problem (1) is that of Sobolev spaces with variable exponent. Recent applications in elasticity [14], non-Newtonian fluid mechanics [15,13,6], or image processing [8], gave rise to a revival of the interest in these spaces, the origins of which can be traced back to the work of Orlicz in the 1930's. An account of recent advances, some open problems, and an extensive list of references can be found in the interesting surveys by Diening [9] and Antontsev [5] (cf. also the work of Kováčik and Rákosník [10], where many of the basic properties of these spaces are established).



The interest of the study of Lebesgue and Sobolev spaces with variable exponent is developed from the proposed model by Chen, Levine and Rao [8] in the application to image processing which the idea behind this application requires the minimization over u of the energy,

$$E(u) = \int_{\Omega} |\nabla u(x)|^{p(x)} + |u(x) - I(x)|^2 dx, \quad (2)$$

where I is given input. Recall that in the constant exponent case, the power $p = 2$ corresponds to isotropic smoothing, which corresponds to minimizing the energy,

$$E_2(u) = \int_{\Omega} |\nabla u(x)|^2 + |u(x) - I(x)|^2 dx. \quad (3)$$

Unfortunately, the smoothing will destroy all small details from the image, so this procedure is not very useful. Where as $p = 1$ gives total variations smoothing which corresponds to minimizing the energy,

$$E_1(u) = \int_{\Omega} |\nabla u(x)| + |u(x) - I(x)|^2 dx. \quad (4)$$

The Benefit of this approach not only preserves edges, it also creates edges where there were none in the original image (the so-called staircase effect).

As the strengths and weaknesses of these two methods for image restoration are opposite, it is a natural to try to combine them. That was the idea of Chen, Levine and Rao [8], looking at E_1 and E_2 suggests that the appropriate energy is $E(u)$ (see 2), where $p(x)$, is a function varying between 1 and 2. This function should be close to 1 where there are likely to be edges, and close to 2 where there are likely not to be edges, and depends on the location x , in the image. In this way the direction and speed of diffusion at each location depends on the local behavior.

We point out that, this model is linked with energy which can be associated to the $p(x)$ -Laplacian operators, i.e.,

$$\Delta_{p(x)} u = -\operatorname{div}(|\nabla u|^{p(x)-2} \nabla u). \quad (5)$$

Moreover, the choice of the exponent yields a variational problem which has an Euler-Lagrange equation, and the solution can be found by solving corresponding evolutionary PDE.

In this paper, we consider a problem with potential applications. This problem has already been treated for constant exponent but it seems to be more realistic to assume the exponent to be variable.

References

- 1.L.Aharouch, Y. Akdim and E. Azroul *Quasilinear degenerate elliptic unilateral problems*, AAA 2005: 1 (2005) 11-31. DOI: 10.1155/AAA.2005.11.



- 2.L.Aharouch, E. Azroul and A. Benkirane *Quasilinear degenerated equations with L^1 datum and without coercivity in perturbation term*, Electronic J.Diff .Equ, (2006), No. **19**, 1-18.
- 3.Y. Akdim, E. Azroul and A. Benkirane, *Existence of Solutions for Quasilinear Degenerated Elliptic Equations*, Electronic J. Diff .Equ, Vol. **2001**, N 71 (2001) pp 1-19.
- 4.Y. Akdim, E. Azroul and A. Benkirane, *Existence Results for Quasilinear Degenerated Equations via Strong Convergence of Truncations*, Revista Matemática Complutense, Madrid, (2004), **17**; N 2, 359-379.
- 5.S. Antontsev, S. Shmarev, *Elliptic equations with anisotropic nonlinearity and nonstandard growth conditions*. In: Handbook of Differential Equations, Stationary Partial Differential Equations, vol. **3**, pp. 1100, Elsevier, 2006.
- 6.S. Antontsev, J. F. Rodrigues, : *On stationary thermorheological viscous flows*. Ann. Univ. Ferrara Sez. VII Sci. Mat. **52** (2006), no. 1, 1936.
- 7.P. Benilan, L. Boccardo, T. Gallouët, R. Gariepy, M. Pierre and J.L. Vazquez, *An L^1 theory of existence and uniqueness of nonlinear elliptic equations*, Ann. Scuola Norm. Sup. Pisa Cl. Sci., **22** (1995), 241273.
- 8.Y. Chen, S. Levine and R. Rao, *Functionals with $p(x)$ -growth in image processing*, <http://www.mathcs.duq.edu/~sel/CLR05SIAPfinal.pdf>.
- 9.L. Diening, P. Hästö and A. Nekvinda, *Open problems in variable exponent Lebesgue and Sobolev spaces*. In: FSDONA04 Proceedings, Drabek and Rakosnik (eds.), pp. 3858, Milovy, Czech Republic, 2004.
- 10.O. Kováčik and J. Rákosník, *On spaces $L^{p(x)}$ and $W^{1,p(x)}$* , Czechoslovak Math. J. **41** (116) (1991), 592-618.
- 11.X.L. Fan, Q.H. Zhang, *Existence of solutions for $p(x)$ -Laplacian Dirichlet problems*, Nonlinear Anal. **52** (2003) 18431852.
- 12.P. Marcellini, *Regularity and existence of solutions of elliptic equations with (p, q) -growth conditions*, J. Differential Equations **90** (1991) 130.
- 13.M. Ružička, *Electrorheological fluids: modeling and mathematical theory*, lecture Notes in Mathematics **1748**, Springer-verlaag, Berlin, 2000.
- 14.V. Zhikov, *Averaging of functionals of the calculus of variations and elasticity theory*, Math. USSR Izvestiya **29** (1987), no. 1, 33-66.
- 15.V. Zhikov, *Meyer-type estimates for solving the nonlinear Stokes system*. Differential Equations **33** (1997), no. 1, 108115.





Numerical Methods for Discontinuous Singularly Perturbed Differential Systems

Marco Berardi¹ and Luciano Lopez²

Department of Mathematics, University of Bari, 70125 Bari, Italy
(E-mail: berardi@dm.uniba.it, lopezl@dm.uniba.it)

Abstract. In this paper we study the numerical solution of singularly perturbed systems with a discontinuous right hand side. We will avoid to consider the associate reduced differential system because often this study leads to wrong conclusions. To handle either the stiffness, due to different scales, or the discontinuity of the vector field we will consider numerical method which are semi-implicit and of low order of accuracy.

Keywords: Singularly perturbed differential systems, Filippov discontinuous systems, numerical methods.

1 Introduction

In this paper we study singularly perturbed systems with a discontinuous right hand side. Differential systems of this type appear in several fields (see for instance [7], [8], [14]) and they have attracted a growing interest also from a theoretical point of view (see for instance [13]).

Let us consider the singularly perturbed differential system in \mathbb{R}^n given the the following form:

$$\begin{cases} x' = f(x, y), & x(0) = x_0, \quad t \in [t_0, T], \\ \epsilon y' = g(x, y), & y(0) = y_0, \end{cases} \quad (1)$$

where usually $0 < \epsilon \ll 1$, while $x : [0, T] \rightarrow \mathbb{R}^{n-m}$ is the *slow* variable, $y : [0, T] \rightarrow \mathbb{R}^m$ is the *fast* variable, the vector field f is discontinuous along a surface Σ while g is sufficiently smooth. Let us suppose that the state space \mathbb{R}^n is split into two subspaces R_1 and R_2 by a surface Σ such that $\mathbb{R}^n = R_1 \cup \Sigma \cup R_2$.

The surface Σ is implicitly characterized by a scalar *event* function $h : \mathbb{R}^n \rightarrow \mathbb{R}$, that is

$$\Sigma = \{(x, y) \in \mathbb{R}^n \mid h(x, y) = 0\} \quad , \quad (2)$$

so that the subspaces R_1 and R_2 are

$$R_1 = \{(x, y) \in \mathbb{R}^n \mid h(x, y) < 0\}, \quad R_2 = \{(x, y) \in \mathbb{R}^n \mid h(x, y) > 0\}. \quad (3)$$

We will assume that $h(x, y)$ is sufficiently smooth and that its gradient $\nabla h(x, y) \neq 0$ for all $(x, y) \in \Sigma$, so that the normal $n(x, y) = \frac{\nabla h(x, y)}{\|\nabla h(x, y)\|}$ to



Σ is well defined. In many practical applications, the function h is actually linear (Σ is a plane).

Let us suppose that the vector field f is discontinuous along Σ , that is:

$$f(x, y) = \begin{cases} f_1(x, y) & \text{when } (x, y) \in R_1 \\ f_2(x, y) & \text{when } (x, y) \in R_2 \end{cases},$$

where f_1 is sufficiently smooth on $R_1 \cup \Sigma$ and f_2 is sufficiently smooth on $R_2 \cup \Sigma$.

Let us assume that for $\epsilon = 0$, the algebraic equation (1.b), that is $g(x, y) = 0$, can be solved for y for all x and that this solution (denoted by $y_0(x)$) satisfies the stability condition:

$$\text{Re Spec } \partial_y g(x, y_0(x)) < -\mu < 0 \quad (4)$$

with a uniform decay rate μ (see [12]).

Furthermore, let us assume that for the reduced system

$$x' = \begin{cases} f_1(x, y_0(x)), & \text{when } h(x, y_0(x)) < 0 \\ f_2(x, y_0(x)), & \text{when } h(x, y_0(x)) > 0 \end{cases} \quad (5)$$

the sufficient conditions for the attractivity of the sub-surface

$$\Sigma_0 = \{(x, y) \in \mathbb{R}^n | y = y_0(x), h(x, y_0(x)) = 0\}, \quad (6)$$

hold.

2 Filippov approach

By setting:

$$z = \begin{bmatrix} x \\ y \end{bmatrix}, \quad F_1(z, \epsilon) = \begin{bmatrix} f_1(z) \\ \frac{1}{\epsilon}g(z) \end{bmatrix}, \quad F_2(z, \epsilon) = \begin{bmatrix} f_2(z) \\ \frac{1}{\epsilon}g(z) \end{bmatrix}, \quad (7)$$

the singularly perturbed discontinuous system (1) may be rewritten in Filippov's form

$$z' = F(z, \epsilon) = \begin{cases} F_1(z, \epsilon), & \text{when } h(z) < 0 \\ F_2(z, \epsilon), & \text{when } h(z) > 0 \end{cases} \quad (8)$$

with initial condition $z_0 = [x(0), y(0)]^T$.

A solution in the sense of Filippov (see [6]) is an absolutely continuous function $z : [0, T] \rightarrow \mathbb{R}^n$ such that $z'(t) \in F(z(t), \epsilon)$ for almost all $t \in [0, T]$, where $F(z(t), \epsilon)$ is the closed convex hull

$$\overline{\text{co}}\{F_1, F_2\} = \{F \in \mathbb{R}^n : F = (1 - \alpha)F_1 + \alpha F_2, \alpha \in [0, 1]\}. \quad (9)$$

Now, suppose $z_0 \in R_1$ (that is $h(z_0) < 0$) and assume that the trajectory of the differential system $z' = F_1(z, \epsilon)$ is directed towards Σ and



reaches it in a finite time. At this point, one must decide what happens next. Loosely speaking, there are two possibilities: (a) we leave Σ and enter into R_2 (*transversal case*); (b) we remain in Σ with a defined vector (*sliding mode*). Filippov devised a very powerful theory which helps to decide what to do in this situation and how to define the vector field during the sliding motion.

Let $z \in \Sigma$ and let $n(z) = \frac{\nabla h(z)}{\|\nabla h(z)\|}$ be the normal to Σ at z . Let $n^T(z)F_1(z, \epsilon)$ and $n^T(z)F_2(z, \epsilon)$ be the projections of $F_1(z, \epsilon)$ and $F_2(z, \epsilon)$ onto the normal direction and suppose that $n^T(z)F_1(z, \epsilon) > 0$. We will exclude the case in which we entry Σ in a tangent way, that is $n^T(z)F_1(z, \epsilon) = 0$ at $z \in \Sigma$.

Transversal Intersection. In case in which, at $z \in \Sigma$, we have

$$[n^T(z)F_1(z, \epsilon)] \cdot [n^T(z)F_2(z, \epsilon)] > 0, \quad (10)$$

then we will leave Σ and enter R_2 with $F = F_2$. Any solution of (8) with initial condition not in Σ , reaching Σ at a time t_1 , and having a transversal intersection there, exists and is unique.

Sliding Mode. Instead, if, at $z \in \Sigma$, we have

$$[n^T(z)F_1(z, \epsilon)] \cdot [n^T(z)F_2(z, \epsilon)] < 0, \quad (11)$$

then we have a so-called attracting sliding mode through z .

When we have (11) satisfied at $z \in \Sigma$, a solution trajectory which reaches z does not leave Σ , and will therefore have to move along Σ . During the sliding motion the solution will continue along Σ with time derivative F_S given by:

$$F_S(z, \epsilon) = (1 - \alpha(z))F_1(z, \epsilon) + \alpha(z)F_2(z, \epsilon). \quad (12)$$

and $\alpha(z)$ such that $F_S(z, \epsilon)$ lies in the tangent plane T_z of Σ at z , that is $n^T(z)F_S(z, \epsilon) = 0$, and this gives

$$\alpha(z) = \frac{n^T(z)F_1(z, \epsilon)}{n^T(z)(F_1(z, \epsilon) - F_2(z, \epsilon))}. \quad (13)$$

Observe that a solution having an attracting sliding mode exists and is unique, in forward time.

As far as the reduced system (5) is concerned, we have to observe that during the sliding mode the Filippov vector field will be

$$f_S(x) = (1 - \alpha_0(x))f_1(x, y_0(x)) + \alpha_0(x)f_2(x, y_0(x)). \quad (14)$$

where

$$\alpha_0(x) = \frac{n_x^T(x)f_1(x, y_0(x))}{n_x^T(x)(f_1(x, y_0(x)) - f_2(x, y_0(x)))}. \quad (15)$$

where $n_x(x) = \frac{\nabla h(x, y_0(x))}{\|\nabla h(x, y_0(x))\|}$.



3 An Example

We observe that while Σ_0 is an attractive surface for the solution of the reduced system (5), on the other hand, the trajectories of the singularly perturbed system (1) could transverse the discontinuity surface Σ , or could slide on it for a certain time interval, or could show a periodic or *chattering* behaviour.

As an example of different behaviours between the initial and reduced system, we consider the following system:

$$\begin{cases} x' = -\text{sign}[\theta x + (1 - \theta)y], \\ \epsilon y' = x - y \end{cases}, \quad (16)$$

where θ is a real parameter ($\theta \neq 0$) and where the discontinuity surface is the line

$$\Sigma = \{(x, y) \in \mathbb{R}^2 \mid h(x, y) = \theta x + (1 - \theta)y = 0\}. \quad (17)$$

A theoretical study of singularly perturbed systems of this kind has been derived in [13]. When $\epsilon = 0$, the reduced system becomes the well known discontinuous system $x' = -\text{sign}[x]$, $x = y$, which has the equilibrium point $(x, y) = (0, 0)$. Such a point is exponentially stable and attractive in finite time. Actually $(0, 0)$ is a *pseudo-equilibrium* because it is an equilibrium of (16) which is on the discontinuity surface Σ . Let us denote

$$F_1(x, y, \epsilon) = \begin{bmatrix} 1 \\ \frac{1}{\epsilon}(x - y) \end{bmatrix}, \quad F_2(x, y, \epsilon) = \begin{bmatrix} -1 \\ \frac{1}{\epsilon}(x - y) \end{bmatrix}, \quad (18)$$

thus, the sliding region will be defined by the points of the line Σ such that $\nabla h^T \cdot F_1 > 0$ and $\nabla h^T \cdot F_2 < 0$, that is the points $(x, y) \in \Sigma$ such that

$$\theta + \frac{1 - \theta}{\epsilon}(x - y) > 0, \quad -\theta + \frac{1 - \theta}{\epsilon}(x - y) < 0.$$

Thus, for $\theta > 0$ and $\theta \neq 1$, assuming $y = \frac{\theta}{\theta - 1}x$, it follows that the sliding region is defined by

$$-\epsilon\theta < x < \epsilon\theta,$$

this means that there is a small neighborhood of $(0, 0)$, on the discontinuity line Σ , on which the solution of (16) sliding reaches the pseudo-equilibrium.

If $\theta < 0$, then $(0, 0)$ is an unstable pseudo-equilibrium, in particular there is a repelling sliding region near the origin and we have a symmetric exponentially stable periodic orbit around the origin switching between the two different vector fields F_1 and F_2 (see [13] for the details). Thus the dynamics of the perturbed system ($\epsilon > 0$) are close the dynamics of the unperturbed system ($\epsilon = 0$) only in a very weak sense (see [5]) and the reduced system cannot be used to study the perturbed one.



4 Numerical methods

The previous example shows that the study of the reduced system ($\epsilon = 0$) could lead to wrong conclusions, in particular certain dynamics of the system could be lost. However, the reduced differential system (5) could be used to approach the discontinuity surface Σ , that is to find an initial point close to Σ from which starting with the numerical solution of the unperturbed differential system.

On the other hand, the numerical solution of discontinuous singularly perturbed problems meets several difficulties. In fact, we need to consider numerical schemes that handle either the discontinuity of the vector field or the stiffness of the solution which arises because of the presence of the small parameter ϵ . To this end we will consider two semi-implicit schemes, one in the class of Predictor-Corrector methods and the other in the class of Rosenbrock methods.

We have adopted a computational approach in which each particular state of the differential system is integrated with an appropriate numerical method, and the event points, where structural changes in the system occur, are located in an accurate way. In [1], this approach is called an *event driven* method (see also the numerical methods in [2], [3]), and the numerical methods we consider will be effective if there are not too many events.

We will be mainly concerned with developing a numerical procedure which will accomplish the following different tasks:

- (i) Integration outside Σ ;
- (ii) Accurate location of points on Σ reached by a trajectory;
- (iii) Check of the transversality or sliding conditions at the points on Σ ;
- (iv) Integration on Σ (sliding mode);
- (v) check of the exit conditions from Σ .

For discretizing the singularly perturbed discontinuous system in (8) we are going to consider schemes (of low order 1) suitable to handle stiff problems. Integration of (8) while the solution remains in R_1 (or R_2) is not different than standard numerical integration of a singularly perturbed differential system (see [10]). Therefore, the only interesting case to consider is when, while integrating the system with F_1 (or F_2), we end up reaching the surface Σ .

Let $z_0 \in R_1$ and consider one step of the implicit Euler method:

$$z_1(\tau) = z_0 + \tau F_1(z_1(\tau), \epsilon), \quad (19)$$

where $\tau > 0$ is the time step of integration. We suppose that τ is sufficiently small in order to avoid situations in which, in the interval $[0, \tau]$, more than one event point occurs. We have to notice that in order to find $z_1(\tau)$ from (19), we have to solve a nonlinear system of n algebraic equation. Let us suppose that τ is such that

$$h(z_0)h(z_1(\tau)) < 0 \quad (20)$$



that is $z_1(\tau)$ is on the other side of Σ . We observe that in the interval $[0, \tau]$ the function $H(\eta) = h(z_1(\eta))$ changes sign. Thus, we may apply a zero finding routine (for instance the bisection or secant method) to determine $\bar{\tau}$, such that $h(z_1(\bar{\tau})) = 0$, that $z_1(\bar{\tau}) \in \Sigma$. The secant methods gives:

$$\eta_{k+1} = \eta_k - \frac{(\eta_k - \eta_{k-1})}{H(\eta_k) - H(\eta_{k-1})} H(\eta_k), \quad k \geq 0,$$

with $\eta_0 = 0$, $\eta_1 = \tau$. However, at each iteration of a such routine a nonlinear system of equations must be solved in order to compute the new vector $z_1(\eta_k)$ required in $H(\eta_k)$ and this could be very expensive.

In order to derive a semi-explicit procedure suitable to treat stiff problems, we consider a predictor-corrector method where the predictor is the Euler explicit method and the corrector is the Euler implicit method, that is

$$\begin{cases} z_1^{(0)}(\tau) = z_0 + \tau F_1(z_0, \epsilon), \\ z_1(\tau) = z_0 + \tau F_1(z_1^{(0)}(\tau), \epsilon), \end{cases} \quad (21)$$

which is equivalent to the explicit formula:

$$z_1(\tau) = z_0 + \tau F_1(z_0 + \tau F_1(z_0, \epsilon), \epsilon). \quad (22)$$

Now, if (20) holds, a simple scalar non linear equation must be solved to find the step size $\bar{\tau}$ for which $z_1(\bar{\tau})$ is on Σ .

A different method we could employ is the semi-explicit Rosenbrock method of order 1:

$$z_1(\tau) = z_0 + \tau t_0, \quad (23)$$

where the vector t_0 is given by

$$[I - \tau J_{F_1}(z_0)] t_0 = F_1(z_0, \epsilon), \quad (24)$$

and where $J_{F_1}(z_0)$ denotes the Jacobian matrix of F_1 at z_0 .

Now, if (20) holds, in the zero finding routine, instead of (23), we may consider the continuous extension of the Rosenbrock method

$$z_1(\sigma\tau) = z_0 + \sigma\tau t_0, \quad \sigma \in (0, 1) \quad (25)$$

where the vector t_0 is again given by (24) but is independent on σ .

An advantage of (23) with respect (21) is that the former does not require the evaluation of the vector field F_1 above Σ , and this property could be necessary in certain discontinuous models.

Once we have a point \bar{z} on Σ , we need to decide if we will need to cross Σ or slide on Σ , that is we will check if

$$[n^T(\bar{z})F_1(\bar{z}, \epsilon)] \cdot [n^T(\bar{z})F_2(\bar{z}, \epsilon)] > 0, \quad (26)$$

or

$$[n^T(\bar{z})F_1(\bar{z}, \epsilon)] \cdot [n^T(\bar{z})F_2(\bar{z}, \epsilon)] < 0, \quad (27)$$



[recall we are supposing that $[n^T(\bar{z})F_1(\bar{z}, \epsilon)] > 0$].

If (26) is satisfied, then we change the vector field and continue to integrate the system:

$$z'(t) = F_2(z(t), \epsilon), \quad z(\bar{\tau}) = \bar{z}, \quad (28)$$

by using the same numerical method used to reach Σ .

5 Integration on Σ

Instead, if (27) is satisfied then we enter an attractive sliding mode, thus we need to integrate the differential Filippov system:

$$z'(t) = F_S(z(t), \epsilon), \quad z(\bar{\tau}) = \bar{z}, \quad (29)$$

where with F_S we indicate the standard Filippov vector field (12).

Since F_S is a linear convex combination of F_1 and F_2 , to integrate (29) we will employ the same method used to reach Σ , that is (21) or (23) where the vector field F_1 is now replaced by F_S .

Now, one step of the Rosenbrock method becomes $z_1(\tau) = z_0 + \tau t_0$, with

$$[I - \tau J_{F_S}(z_0)] t_0 = F_S(z_0, \epsilon) \quad (30)$$

where $J_{F_S}(z_0)$ denotes the Jacobian matrix of F_S at $z_0 \in \Sigma$. Because of the form of F_S , this Jacobian matrix J_{F_S} could be very expensive to evaluate and a free-Jacobian procedure has to be used in the solution of the linear system (30) by means of iterative or Krylov type procedures (see [11]).

We observe that when we integrate on Σ , usually, the numerical solution given by (21) or (23) leaves the surface Σ and a projection is necessary to return on Σ . The projection on Σ may be done in the standard way (e.g., see [4], [9]). If \hat{z} is a point close to Σ , then the projected vector $z = P(\hat{z})$ on Σ is the solution of the following constrained minimization problem

$$\min_{z \in \Sigma} g(z), \quad g(z) = \frac{1}{2}(\hat{z} - z)^T(\hat{z} - z).$$

By using the Lagrange's multiplier's method, we have to find the root of

$$G(z, \lambda) = \begin{pmatrix} \nabla g(z) + \lambda \nabla h(z) \\ h(z) \end{pmatrix}, \quad \lambda \in \mathbb{R},$$

and we can apply Newton's method to find the root of $G(z, \lambda) = 0$.

On the other hand, if Σ is flat, that is $h(z) = a^T z + b$ linear with respect to z , then the numerical solution given by (21) lies on Σ while the one obtained by (23) does not.

Theorem 1. *Let us assume Σ given by $h(z) = a^T z + b$, and suppose that $z_0 \in \Sigma$. Then z_1 given by (21) lies on Σ while z_1 given by (23) does not.*



Proof. Let us consider the numerical solution

$$z_1 = z_0 + \tau F_S(z_0 + \tau F_S(z_0, \epsilon), \epsilon) . \quad (31)$$

We notice that the predicted vector $z_0 + \tau F_S(z_0, \epsilon)$ remains on Σ since it has been obtained by an explicit method which preserves linear invariants (see [9]). Thus, it follows that

$$a^T z_1 + b = a^T [z_0 + \tau F_S(z_0 + \tau F_S(z_0, \epsilon), \epsilon)] + b = a^T z_0 + b = 0 ,$$

since $a^T F_S(z_0 + \tau F_S(z_0, \epsilon)) = 0$ being a^T the normal vector of Σ .

Now, we would like to see if $a^T z_1 + b = 0$ when z_1 is the numerical solution obtained by (23). Then it follows that

$$\begin{aligned} a^T z_1 + b &= a^T (z_0 + \tau [I - \tau J(z_0)]^{-1} F_S(z_0, \epsilon)) + b = \\ &= a^T z_0 + b + \tau a^T [I - \tau J(z_0)]^{-1} F_S(z_0, \epsilon) , \end{aligned}$$

thus z_1 is on Σ only if $a^T [I - \tau J(z_0)]^{-1} F_S(z_0, \epsilon) = 0$. We observe that $a^T F_S(z_0, \epsilon) = 0$, and that for τ sufficiently small we have

$$[I - \tau J]^{-1} = I + \tau J + \frac{\tau^2}{2} J^2 + \frac{\tau^3}{6} J^3 + \dots$$

thus z_1 is on Σ if and only if $JF_S = F_S$, that in general is not true.

Thus, usually, to remain on Σ a projection on it is required. While we integrate on Σ , we will monitor if we have to continue sliding on it, or if we need to leave Σ . Once the point z_1 on Σ has been computed, we need to check if the sliding condition

$$[n^T(z_1)F_1(z_1, \epsilon)] \cdot [n^T(z_1)F_2(z_1, \epsilon)] < 0 , \quad (32)$$

is satisfied or if this product changes sign, that is

$$[n^T(z_1)F_1(z_1, \epsilon)] \cdot [n^T(z_1)F_2(z_1, \epsilon)] > 0 , \quad (33)$$

If (32) holds then we continue to integrate on Σ . On the other hand, if (33) holds then we have to determine $\bar{\tau}$ (and hence $z_1(\bar{\tau})$) such that the previous product vanishes. Thus, starting with $z_1(\bar{\tau})$, we exit the surface Σ with vector field $F_2(z_1(\bar{\tau}), \epsilon)$.

6 Numerical tests

In this section we report the numerical simulations of some singularly perturbed discontinuous systems, obtained by using the numerical methods studied. We will report the results obtained by **Matlab** codes using both the

predictor-corrector method in (21) and the Rosenbrock method in (23) with sufficiently small time step τ .

Example 1. Here we consider the numerical solution of the system in (16), with $\epsilon = 0.001$, by means of the numerical methods proposed in the previous section. Figure 1 concerns with the case $\theta > 0$ (we have taken $\theta = 0.9$ and denoted by '*' the initial value). We can see that the numerical solution first crosses the discontinuity surface Σ (denoted by the red color), then begins to slide on Σ until to reach the pseudoequilibrium $(0, 0)$.

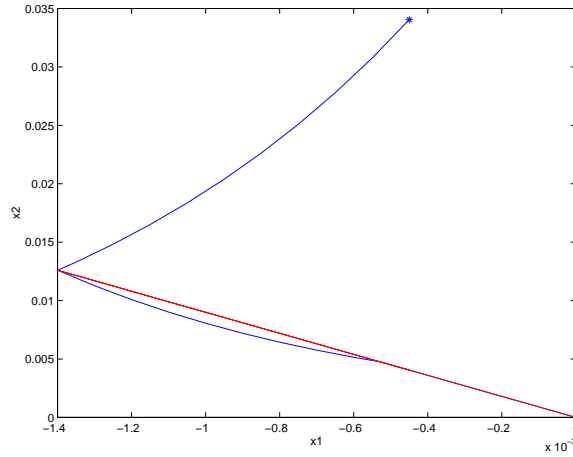


Fig. 1. Example 1. Case $\theta = 0.90$.

Figure 2 concerns with the case $\theta < 0$ ($\theta = -0.9$). We can see that the numerical solution tends to an exponentially stable periodic orbit around the origin while the vector field switches between the two different vector fields F_1 and F_2 . In Figure 3 we have reported the exponentially stable periodic solution of the system.

Example 2. Let us consider the following discontinuous differential system:

$$\begin{pmatrix} x'_1 \\ x'_2 \end{pmatrix} = \begin{cases} \mu x_1 - \omega x_2 - (x_1^2 + x_2^2)x_1 \\ \omega x_1 + \mu x_2 - (x_1^2 + x_2^2)x_2 \end{cases}, \quad \text{when } h(x_1, x_2) \geq 0 \quad (34)$$

or

$$\begin{pmatrix} x'_1 \\ x'_2 \end{pmatrix} = \begin{cases} 1 \\ 0 \end{cases}, \quad \text{when } h(x_1, x_2) < 0 \quad (35)$$

[μ and ω positive constants] while the switching line is given by $h(x_1, x_2) = x_1 + 1$, therefore $\nabla^T h(x) = [1 \ 0]$. Using our notation, we have:

$$f_1 = \begin{bmatrix} 1 \\ 0 \end{bmatrix}, \quad f_2 = \begin{bmatrix} \mu x_1 - \omega x_2 - (x_1^2 + x_2^2)x_1 \\ \omega x_1 + \mu x_2 - (x_1^2 + x_2^2)x_2 \end{bmatrix}, \quad (36)$$

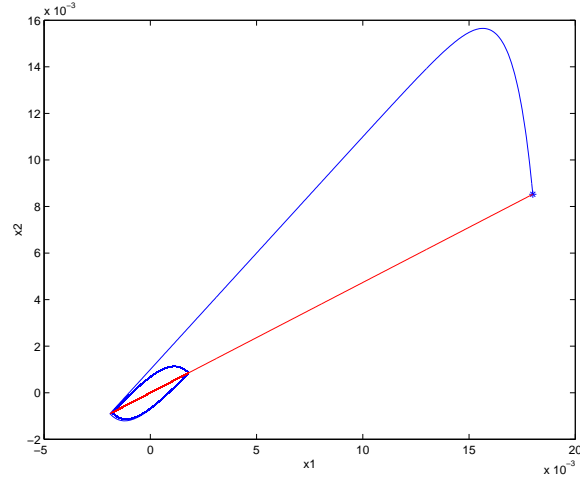


Fig. 2. Example 1. Case $\theta < 0$.

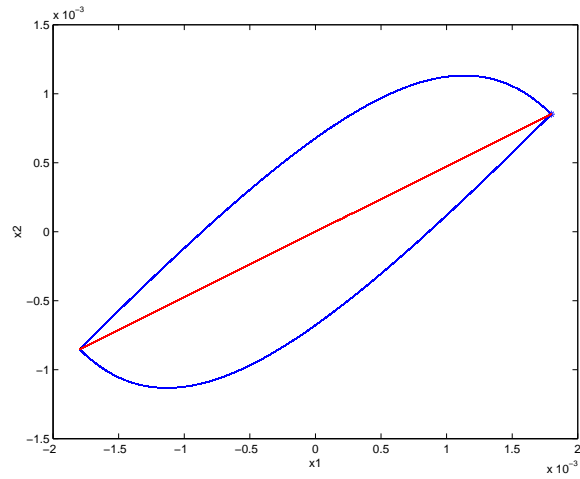


Fig. 3. Example 1. Case $\theta < 0$: stable periodic solution.

and observe that $\nabla^T h \cdot f_1 = 1 > 0$. Hence, when $\mu > 1$, the attractive sliding region S_R is the segment on the line $x_1 = -1$ for which $\nabla^T h \cdot f_2 < 0$, that is $S_R = \{(-1, x_2) \in \mathbb{R}^2 \mid -\mu - \omega x_2 + (1 + x_2^2) < 0\}$. In Figure 4 we report the exponentially stable periodic solution of (35) obtained for $\mu = 1.5$ and $\omega = 1$ by our numerical methods.

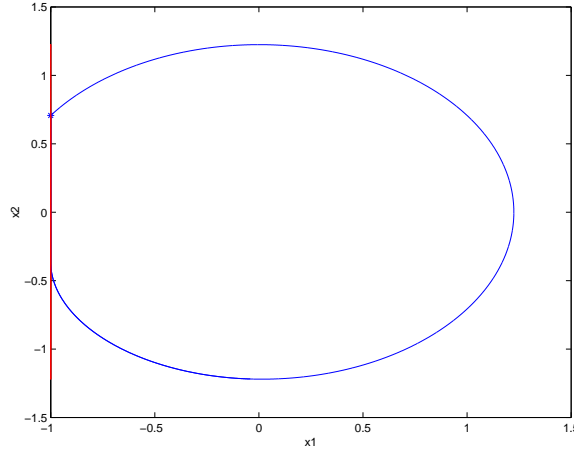


Fig. 4. Example 2. Stable periodic solution.

Now, let us consider the singularly perturbed discontinuous system:

$$\begin{pmatrix} x'_1 \\ x'_2 \\ \epsilon x'_3 \end{pmatrix} = \begin{cases} x_1 - \omega x_2 - (x_1^2 + x_2^2)x_1 \\ \omega x_1 + \mu x_2 - (x_1^2 + x_2^2)x_2 \\ \epsilon[\mu x_1 - \omega x_2 - (x_1^2 + x_2^2)x_1] + x_1 - x_3 \end{cases}, \quad h(x_1, x_2, x_3) \geq 0 \quad (37)$$

while

$$\begin{pmatrix} x'_1 \\ x'_2 \\ \epsilon x'_3 \end{pmatrix} = \begin{cases} 1 \\ 0 \\ \epsilon[\mu x_1 - \omega x_2 - (x_1^2 + x_2^2)x_1] + x_1 - x_3 \end{cases}, \quad h(x_1, x_2, x_3) < 0 \quad (38)$$

where the last component of the vector field is continuous while the previous two components are discontinuous with respect the line:

$$\Sigma = \{(x_1, x_2, x_3) \in \mathbb{R}^3 \mid h(x_1, x_2, x_3) = \theta x_1 + (1 - \theta)x_3 = 0\}. \quad (39)$$

The reduced system ($\epsilon = 0$) is the one in (34)-(35). A theoretical study of the system (37)-(38) may be found in [13]. In Figure 5 we report the periodic solution of the singularly perturbed system (37)-(38) for $\epsilon = 0.01$, $\mu = 1.5$, $\omega = 1$ and assuming a positive value of the parameter θ ($\theta = 0.5$). A zoom of the solution near the sliding segment of the reduced system may be seen in Figure 6. Instead, in Figure 7 the periodic solution of (37)-(38) with $\theta = -0.5$ is shown, while in Figure 8 we show the chattering behaviour of the solution near the sliding segment of the reduced system.

References

1. V. Acary and B. Brogliato. *Numerical Methods for Nonsmooth Dynamical Systems. Applications in Mechanics and Electronics*. Lecture Notes in Applied

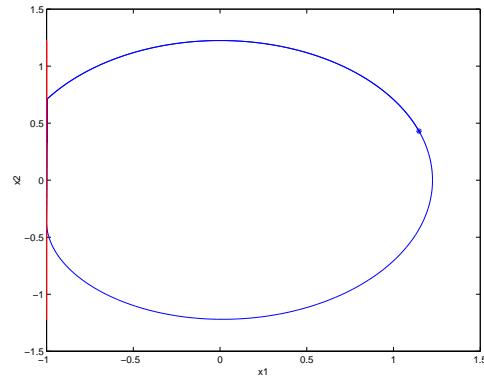


Fig. 5. Example 2. Case $\theta = 0.5$. Periodic solution.

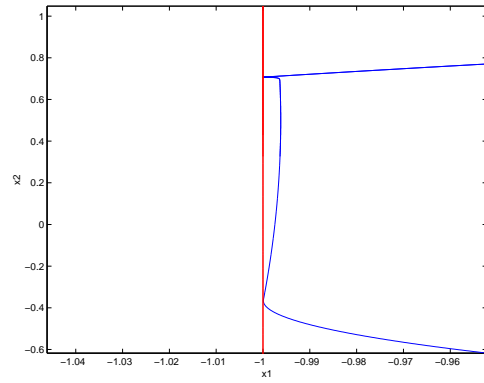


Fig. 6. Example 2. Case $\theta = 0.5$. Zoom of the solution.

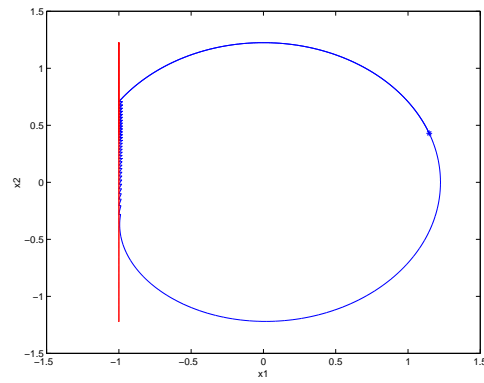


Fig. 7. Example 2. Case $\theta = -0.5$. Periodic solution.

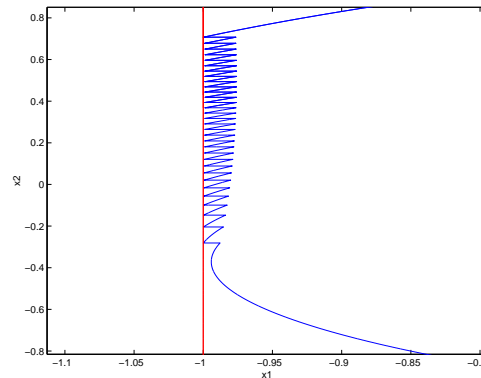


Fig. 8. Example 2. Case $\theta = -0.5$. Zoom of the solution.

- and Computational Mechanics. Springer-Verlag, Berlin, 2008.
2. L. Dieci and L. Lopez. Sliding motion in Filippov differential systems: Theoretical results and a computational approach. *SIAM J. Numer. Anal.*, 47:2023–2051, 2009.
 3. L. Dieci and L. Lopez. Numerical Solution of Discontinuous Differential Systems: Approaching the Discontinuity from One Side. *Applied Numerical Mathematics*, Submitted, 2011.
 4. E. Eich-Soellner and C. Fuhrer. *Numerical Methods in Multibody Dynamics*. B.G. Teubner Stuttgart, Germany, 1998.
 5. N. Fenichel. Geometric singular perturbation theory for ordinary differential equations. *Journal of Differential Equations*, 31:53–98, 1979.
 6. A.F. Filippov. *Differential Equations with Discontinuous Right-Hand Sides*. Mathematics and Its Applications, Kluwer Academic, Dordrecht, 1988.
 7. L. Fridman. Singularly perturbed analysis to chattering in relay control systems. *IEEE Transactions on Automatic Control*, 47:2079–2084, 2002.
 8. L. Fridman. Slow periodic motions in variable structure systems. *Int. J. of Systems Science*, 33:1145–1155, 2002.
 9. E. Hairer, C. Lubich, and G. Wanner. *Geometric Numerical Integration: structure-preserving algorithms for ordinary differential equations*. Springer-Verlag, Berlin, 2006.
 10. E. Hairer, C. Lubich, and G. Wanner. *Solving Ordinary Differential Equations II: Stiff Problems. Second revised Edition*. Springer-Verlag, Berlin, 2010.
 11. D.A. Knoll and D.E. Keyes. Jacobian-free Newton Krylov methods: A survey of approaches and applications. *Journal of Computational Physics*, 193:357–397, 2004.
 12. R.E. O’Maley. *Singular Perturbation Methods for Ordinary Differential Equations*. Springer-Verlag, New York, 1999.
 13. J. Sieber and P. Kowalczyk. Small-scale instabilities in dynamical systems with sliding. *Physica D*, 239:44–57, 2010.
 14. A. Soto-Cota, L.M. Fridman, A.G. Loukianov, and J.M. Canedo. Variable structure control of synchronous generator: singularly perturbed analysis. *Inter. J. of Control*, 79:1–13, 2006.





BetaBoop Brings in Chaos

Maria de Fátima Brilhante,¹ Maria Ivette Gomes² and Dinis Pestana³

¹ Universidade dos Açores and CEAUL, Ponta Delgada, Açores, Portugal
(E-mail: fbrilhante@uac.pt)

² Universidade de Lisboa and CEAUL, Lisboa, Portugal
(E-mail: ivette.gomes@fc.ul.pt)

³ Universidade de Lisboa and CEAUL, Lisboa, Portugal
(E-mail: dinis.pestana@fc.ul.pt)

Abstract. The Verhulst differential equation $\frac{d}{dt}N(t) = r N(t) (1 - N(t))$ and its logistic parabola difference equation counterpart $x_{t+1} = \alpha x_t (1 - x_t) I_{(0,1)}(x_t)$, $\alpha \in [0, 4]$, are tied to sustainable growth. We investigate the implications of considering $1 - N(t)$ the linear truncation of the MacLaurin expansion of $-\ln N(t)$, or $N(t)$ the linear truncation of $-\ln(1 - N(t))$, i.e. of curbing down either the retroaction factor $1 - N(t)$ or the growing factor $N(t)$, which leads to Gumbel extreme value population for maxima or minima, respectively. More generally, we consider $\frac{d}{dt}N(t) = r N(t) (-\ln N(t))^{1+\gamma}$ (or, alternatively, $\frac{d}{dt}N(t) = r (-\ln(1 - N(t)))^{1+\gamma} (1 - N(t))$) and its difference equation counterpart. Simple extensions of the beta densities arise naturally in this context, and we discuss a *BetaBoop*(p, q, P, Q), $p, q, P, Q > 0$ family of probability density functions, that for $P = Q = 1$ reduces to the usual *Beta*(p, q) family.

Keywords: Population dynamics and chaos, extremal models, beta family.

1 Introduction

The rationale of the Verhulst population dynamics model

$$\frac{d}{dt}N(t) = r N(t) (1 - N(t)) \quad (1)$$

is well-known: due to the malthusian reproduction rate $r > 0$, $r N(t)$ implies growth, but on the other hand the retroaction term $-r N^2(t)$ slows down the growth impetus, and ultimately dominates, an action that is often interpreted in terms of sustainability. Hence the logistic solution of (1), $N(t) = 1/(1 + e^{-rt})$ (normalized so that $N(t)$ is a probability distribution function), is often tied to the idea of sustainable population dynamics growth.

Using Euler's algorithm, with an appropriate factor s , the equation (1) can be rewritten as

$$N(t+1) = N(t) + sr N(t) (1 - N(t)) \iff x_{t+1} = \alpha x_t (1 - x_t) \quad (2)$$

where $x_t = sr N(t)/(sr + 1)$, $\alpha = 1 + sr$; if $\alpha \in (0, 4)$, $x_t \in (0, 1) \implies x_{t+1} \in (0, 1)$.



Due to its connection to the logistic curve, $\alpha x(1-x)I_{(0,1)}(x)$ is sometimes referred to as logistic parabola. Observe that, with the notation $X_{p,q} \curvearrowright Beta(p,q)$, $\alpha x(1-x)I_{(0,1)}(x) = \frac{\alpha}{6} f_{X_{2,2}}(x)$, where $f_{X_{2,2}}(x) = 6x(1-x)I_{(0,1)}(x)$ is the probability density function of $X_{2,2} \curvearrowright Beta(2,2)$.

The fact that Euler's algorithm transforms the logistic differential equation in the difference equation model $x_{n+1} = \alpha x_n(1-x_n)$ had an important impact in the recognition that bifurcations, fractality, and ultimate chaos when the reproduction rate r is explosive and sustainability fails, were indeed important tools in modeling population dynamics.

As the Verhulst model is closely tied to the $Beta(2,2)$ probability density function, Aleixo *et al.* [1], [2], investigated the population dynamics of its natural extensions tied to general $Beta(p,q)$ models. Explicit solutions of the differential equation $\frac{d}{dt}N(t) = rN^{p-1}(t)(1-N(t))^{q-1}$ exist only for some (p,q) other than $(2,2)$ — for instance, $4e^{rt}/(1+e^{rt})^2$ is the solution of $\frac{d}{dt}N(t) = rN(t)\sqrt{1-N(t)}$ — but using appropriate software (we used *Mathematica* 7) numerical approximations of the solutions of practical problems are easily worked out.

As $\ln N(t) = -\sum_{k=1}^{\infty} (1-N(t))^k/k$, the factor $1-N(t)$ in (1) may be looked at as the linear truncation of $-\ln N(t)$. In the differential equation

$$\frac{d}{dt}N(t) = rN(t)(-\ln N(t)), \quad (3)$$

the retroaction factor $-\ln N(t)$ is much lighter than $1-N(t)$, and hence it is not surprising that the solution of (3), $N(t) = e^{-e^{-rt}}$ (once again normalized to be a probability distribution function) is one of the extreme value laws for maxima, namely the Gumbel law.

On the other hand $\ln(1-N(t)) = -\sum_{k=1}^{\infty} N^k(t)/k$, and considering that the growing factor $N(t)$ in (1) is the linear approximation of $-\ln(1-N(t))$, we may regard (1) as an approximation of

$$\frac{d}{dt}N(t) = r(-\ln(1-N(t)))(1-N(t)) \quad (4)$$

whose solution, once again normalized, is the Gumbel extreme value distribution for minima, $N(t) = 1 - e^{-e^{-rt}}$, which makes sense since in this case we curbed down the growing factor.

Pestana *et al.* [4] investigated $\frac{d}{dt}N(t) = rN(t)(-\ln N(t))$ and its discretization counterpart $x_{t+1} = sr x_t(-\ln x_t)$ in modeling extremal growth rate, as observed in the dynamics of cancer cells populations.

The generalization $f_{p,Q}(x) = \frac{p^Q}{\Gamma(Q)} x^{p-1}(-\ln x)^{Q-1}I_{(0,1)}(x)$ of the beta densities, has been introduced by Brillhante *et al.* [3]. In Section 2 we discuss the behavior of $x_{t+1} = r x_t(-\ln x_t)I_{(0,1)}(x)$, the more general differential equation $\frac{d}{dt}N(t) = rN(t)(-\ln N(t))^{1+\gamma}$ and its connection to extreme value laws, as well as the behavior of $x_{t+1} = sr x_t(-\ln x_t)^{1+\frac{1}{\gamma}}I_{(0,1)}(x)$. In Section



3 we introduce a new extension of the beta densities, namely

$$f_{p,q,P,Q}(x) = c x^{p-1} (1-x)^{q-1} (-\ln(1-x))^{P-1} (-\ln x)^{Q-1} I_{(0,1)}(x), \quad (5)$$

$p, q, P, Q > 0$, and a general discussion on modeling population dynamics via differential equations/difference equations, questioning whether chaos is in fact an appropriate framework in the description of evolution of populations.

2 Extreme value laws and population dynamics

As observed in Section 1, the Gumbel distribution function for maxima, $N(t) = e^{-e^{-rt}}$, is a solution of the differential equation $\frac{d}{dt}N(t) = r N(t) (-\ln N(t))$, and the Gumbel distribution function for minima, $N^*(t) = 1 - e^{-e^{rt}}$, is a solution of the differential equation $\frac{d}{dt}N^*(t) = r (-\ln(1 - N^*(t))) (1 - N^*(t))$. We now consider difference equations closely tied to those differential equations, i.e., we assume that there exists an appropriate c such that

$$N(t+1) = N(t) + cN(t) (-\ln N(t)) \iff N(t+1) = -cN(t) \ln \left(\frac{N(t)}{e^{\frac{1}{s}}} \right),$$

and we obtain the difference equation,

$$x_{t+1} = c x_t (-\ln x_t), \quad (6)$$

closely associated to (3). As long as $x_t \in (0, 1)$, if $c \in (0, e)$ we also have $x_{t+1} \in (0, 1)$. The stationary solutions of (6) are $x_{t+1} = x_t = x_0$ with $x_0 = 0$ or $x_0 = e^{-\frac{1}{c}}$. In view of the stability criterion for the stationary solutions, $|c(-\ln x - 1)| < 1$, and hence the stationary solution $x_0 = e^{-\frac{1}{c}}$ is stable for $0 < c < 2$, cf. Fig. 1

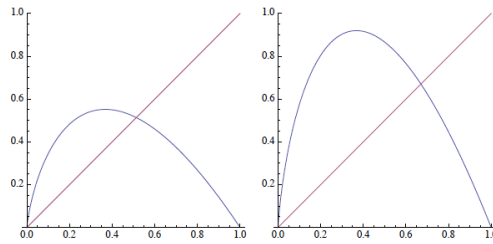


Fig. 1. Left: $1.5 x_t (-\ln x_t)$; right: $2.5 x_t (-\ln x_t)$.

Using in *Mathematica* 7 the output of the instructions

```
Clear[f, x]
f[c_][x_] := c x * (-Log[x]) // N
```



```
x[c_][n_] := x[c][n] = f[c][x[c][n - 1]] // N
x[c_][0] := 0 // N;
tb = Table[{c, x[c][n]}, {c, .1, Exp[1], .01}, {n, 1000, 1300}];
Short[tb]
```

as input for the instructions

```
tb2 = Flatten[tb, 1];
ListPlot[tb]
```

we obtain the graph in Fig. 2, exhibiting bifurcations for $c \geq 2$, and ultimately chaos, as expected from the observations above.

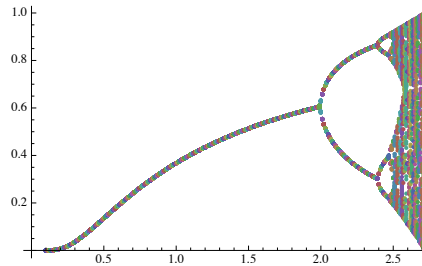


Fig. 2. Bifurcation diagram, solving $x = f(c, x) = cx(-\ln x)$, $c \in (0, e)$, using the fixed point method.

As we have discussed previously, the Gumbel distribution for minima $N(t) = 1 - e^{-e^{-rt}}$ is a solution for the differential equation $\frac{d}{dt}N^*(t) = r(-\ln(1 - N^*(t)))(1 - N^*(t))$, which is tied to the difference equation $x_{t+1} = c(-\ln(1 - N(t)))(1 - N(t))$. Fig. 3 is the simile of Fig. 2 for this case.

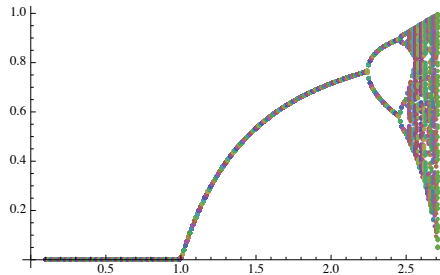


Fig. 3. Bifurcation diagram, solving $x = f(c, x) = c(-\ln(1 - x))(1 - x)$, $c \in (0, e)$, using the fixed point method.

A more general situation involves the study of the differential equations



- $\frac{d}{dt}N(t) = rN(t)(-\ln N(t))^{1+\frac{1}{\gamma}}$, whose solution for $\gamma > 0$ is (again in standardized form) the Fréchet distribution function for maxima $N(t) = e^{-(\frac{r}{\gamma}x)^{-\gamma}} I_{[0,\infty)}(t)$, and whose solution for $\gamma < 0$ is the Weibull distribution function for maxima $N(t) = e^{-(\frac{r}{\gamma}t)^{\gamma}} I_{(-\infty,0)}(t) + 1 I_{[0,\infty)}(t)$.
- $\frac{d}{dt}N(t) = rN(t)(-\ln N(t))^{1+\frac{1}{\gamma}}$, whose solution for $\gamma > 0$ is the Fréchet distribution for minima, and for $\gamma < 0$ is the Weibull distribution function for minima.

Fig. 4 and Fig. 5 illustrate the dynamical behavior when solving by the fixed point method the difference equations closely associated to the above differential equations, namely $x_{t+1} = cx_t(-\ln x_t)^{1+\frac{1}{\gamma}}$ for $\gamma = 1$ (Fréchet-1) and $\gamma = -2$ (Weibull-0.5).

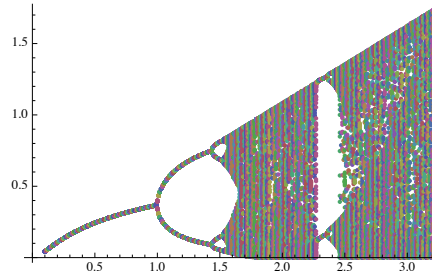


Fig. 4. Bifurcation diagram, solving $x = f(c, x) = cx(-\ln x)^2$ using the fixed point method.

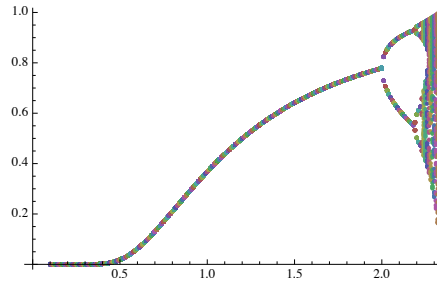


Fig. 5. Bifurcation diagram, solving $x = f(c, x) = cx(-\ln x)^{0.5}$ using the fixed point method.

Remark 1. Considering the General Extreme Value (GEV) distribution for maxima, $G_{\gamma^*}(t) = e^{-(1+\gamma^*t)^{-1/\gamma^*}}$, $1 + \gamma^*t > 0$, it is obvious, from $(1 + \gamma^*t)^{-1/\gamma^* - 1} = ((1 + \gamma^*t)^{-1/\gamma^*})^{\frac{1/\gamma^* + 1}{1/\gamma^*}} = (-\ln G_{\gamma^*}(t))^{1+\gamma^*}$,



that G_{γ^*} satisfies the differential equation

$$\frac{d}{dt}G_{\gamma}(t) = G_{\gamma}(t) (-\ln G_{\gamma}(t))^{1+\frac{1}{\gamma}}, \quad \gamma = \frac{1}{\gamma^*}.$$

In the GEV representation, a shape parameter $\gamma^* > 0$ corresponds to the Fréchet- $\frac{1}{\gamma^*}$, $\gamma^* < 0$ corresponds to the Weibull- $\frac{1}{|\gamma^*|}$, and $\gamma^* \rightarrow 0$ corresponds to the Gumbel.

The similarity of $\frac{d}{dt}N(t) = rN(t)(-\ln N(t))^{1+\frac{1}{\gamma}}$ and $\frac{d}{dt}N(t) = r(-\ln(1-N(t)))^{1+\frac{1}{\gamma}}(1-N(t))$ comes from the fact that stable distributions G for maxima (either Gumbel, or Fréchet or Weibull) and the corresponding stable distributions G^* for minima are tied through the relationship $G^*(x) = 1 - G(-x)$.

3 The BetaBoop family

Brilhante *et al.* [3] extensively studied the family of probability density functions $f_{p,Q}(x) = \frac{p^Q}{\Gamma(Q)} x^{p-1} (-\ln x)^{Q-1} I_{(0,1)}(x)$, $p, Q > 0$, and their relevance in population studies. Denote $X_{p,Q} \sim \text{Betinha}(p, Q)$, $p, Q > 0$, the random variable whose probability density function is $f_{p,Q}(x)$, given above.

In fact, $4x(-\ln x)I_{(0,1)}(x)$, tied to the Gumbel model, is the case $p = Q = 2$ in this family, just as $6x(1-x)$, tied to the logistic parabola and the Verhulst population model, is the case $p = q = 2$ of the $\text{Beta}(p, q)$ family of probability density functions, whose dynamical behavior has been studied in depth in Aleixo *et al.* [1], [2], and references therein. This new family provides difference models whose associated differential models have as solution, among others, the stable distributions for maxima.

In the previous section we have seen that the probability density function of random variables $Y_{p,q} = 1 - X_{q,P}$, with $q = 2$, are connected to difference equations associated to differential equations having as solutions the stable distributions for minima.

In fact, in view of Hölder's inequality, the function $x^{p-1}(1-x)^{q-1}(-\ln(1-x))^{P-1}(-\ln x)^{Q-1}I_{(0,1)}(x)$ is integrable for every $p, q, P, Q > 0$, and hence there exists $c \in (0, \infty)$ such that $f_{p,q,P,Q}(x)$, in (5), is a probability density function. We denote the corresponding random variable $X_{p,q,P,Q} \sim \text{BetaBoop}(p, q, P, Q)$. Observe that $\text{BetaBoop}(p, q, 1, 1)$ is the same as $\text{Beta}(p, q)$, and $\text{BetaBoop}(p, 1, P, 1)$ is the same as $\text{Betinha}(p, P)$.

Betty Boop brought in chaos to the American Board of Censorship — sorry, we were dreaming of Betty Boop and Jessica Rabbit, and what we really meant to say is $\text{BetaBoop}(p, q, P, Q)$ brings in chaos, in the sense that the fixed point solution of equations of the type $x = c x^{p-1}(1-x)^{q-1}(-\ln(1-x))^{P-1}(-\ln x)^{Q-1}$ exhibit all the problems first encountered in the numerical solution of the case $p = q = 2$, $P = Q = 1$. In Fig. 6 we illustrate this for $p = q = P = Q = 1.5$, and in Fig. 7 for $p = q = 1$, $P = Q = 3$

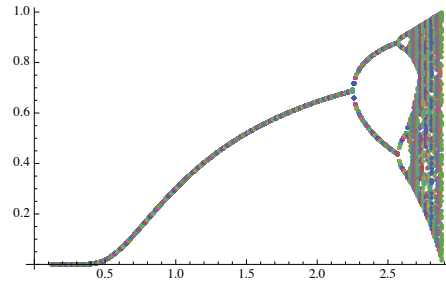


Fig. 6. Bifurcation diagram, solving $x = f(c, x) = c(x(1-x)(-\ln(1-x))(-\ln x))^{0.5}$ using the fixed point method.

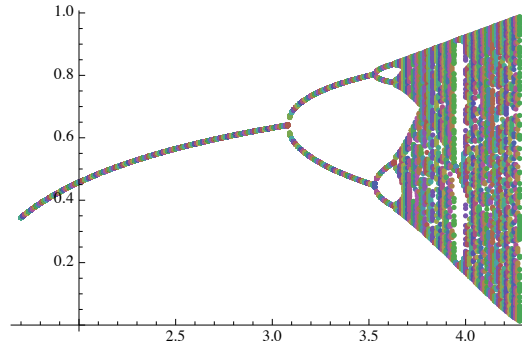


Fig. 7. Bifurcation diagram, solving $x = f(c, x) = c((-\ln x)(-\ln(1-x)))^2$ using the fixed point method.

In fact, many other generalizations of the logistic parabola $f_c(x) = cx(1-x)$ are potentially interesting in modeling population dynamics, as far as they reflect recognizable characteristics. For instance, the linear truncation of $e^{-x} \approx (1-x)$ shows that $cx e^{-x} I_{(0,1)} \approx c^* x(1-x) I_{(0,1)}$. In Fig. 8 we represent the bifurcation diagram corresponding to the difference equation $x_{t+1} = cx e^{-x}$, modeling extremely slow growth.

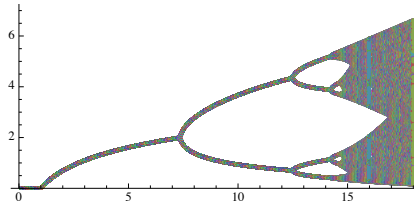


Fig. 8. Bifurcation diagram, solving $x = f(c, x) = cx e^{-x}$ using the fixed point method.



Finally, let us remark that there are grounds to argue that the chaos map (for instance $x_{t+1} = cx_t(-\ln x_t)$) is not an appropriate discrete equivalent of the original differential equation (for that example, $\frac{d}{dt}N(t) = rN(t)(-\ln N(t))$), inasmuch as the chaos map implies bifurcations and ultimately chaos, inexistent in the original differential equation. An interesting point is that if we consider that the retroaction acts at time $t+1$, we obtain a difference equation $x_{t+1} = cx_t(-\ln x_{t+1})$, that has the same stationary solutions as the chaos map $x_{t+1} = cx_t(-\ln x_t)$, but does not exhibit bifurcation and chaos. In fact, from $x_{t+1} = cx_t(-\ln x_{t+1})$ we get a solution $f_c(x) = cx W\left(\frac{1}{cx}\right) I_{(0,\infty)}$, where $W(x)$ is the Logarithmic Product function. Fig. 9 below shows that $cx W\left(\frac{1}{cx}\right) I_{(0,\infty)}$ is a distribution function, that may serve as a non-stable approximation, in the right tail, to the Gumbel distribution.

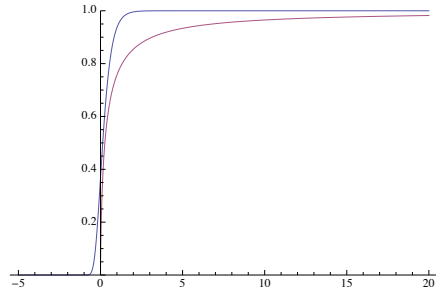


Fig. 9. $cx W\left(\frac{1}{cx}\right) I_{(0,\infty)}$ approximation of $e^{-e^{-cx}}$

Research partially supported by FCT/OE and PTDC.

References

1. S. Aleixo, J.L. Rocha, and D. Pestana. Beta(p,q)-Cantor Sets: Determinism and Randomness. In C.H. Skiadas, I. Dimotikalis and C. Skiadas, editors, *Chaos Theory: Modeling, Simulation and Applications*, Singapore, 2011. World Scientific (in press).
2. S. Aleixo, J.L. Rocha, and D. Pestana. Populational Growth Model Proportional to Beta Densities. In M.M. Peixoto, A.A. Pinto, and D.A.J. Rand, editors, *Dynamics, Games and Science, in honour of Mauricio Peixoto and David Rand*, vol II, Ch. 5, p. 79–95, New York 2011. Springer Verlag.
3. M.F. Brilhante, D. Pestana, and M.L. Rocha. Betices, *Boletim da Sociedade Portuguesa de Matemática*, 2011. (in press).
4. D. Pestana, S. Aleixo, and J.L. Rocha. Regular variation, paretian distributions, and the interplay of light and heavy tails in the fractality of asymptotic models. In C.H. Skiadas, I. Dimotikalis and C. Skiadas, editors, *Chaos Theory: Modeling, Simulation and Applications*, Singapore, 2011. World Scientific, 309–316.